Title

Electrolyte-Induced Surface Transformation and Transition-Metal Dissolution of Fully Delithiated $LiNi_{0.8}Co_{0.15}Al_{0.05}O_2$

Journal

Langmuir, 33(37)

ISSN

0743-7463

Authors

Faenza, Nicholas V
Lebens-Higgins, Zachary W
Mukherjee, Pinaki
et al.

Publication Date

2017-09-19

DOI

10.1021/acs.langmuir.7b00863

Peer reviewed

LANGMUIR

Article

pubs.acs.org/Langmuir

Electrolyte-Induced Surface Transformation and Transition-Metal Dissolution of Fully Delithiated $LiNi_{0.8}Co_{0.15}Al_{0.05}O_2$

Nicholas V. Faenza,*[,†] Zachary W. Lebens-Higgins,[‡] Pinaki Mukherjee,[§] Shawn Sallis,[∥] Nathalie Pereira,[†] Fadwa Badway,[†] Anna Halajko,[†] Gerbrand Ceder,[⊥] Frederic Cosandey,[§] Louis. F. J. Piper,[‡,∥] and Glenn G. Amatucci[†]

[†]Energy Storage Research Group, Department of Materials Science and Engineering, Rutgers University, North Brunswick, New Jersey 08902, United States

[‡]Department of Physics, Applied Physics and Astronomy and [∥]Department of Materials Science and Engineering, Binghamton University, Binghamton, New York 13902, United States

[§]Department of Materials Science and Engineering, Rutgers University, Piscataway, New Jersey 08854, United States

[⊥]Department of Materials Science and Engineering, University of California, Berkeley, California 94720, United States

Supporting Information

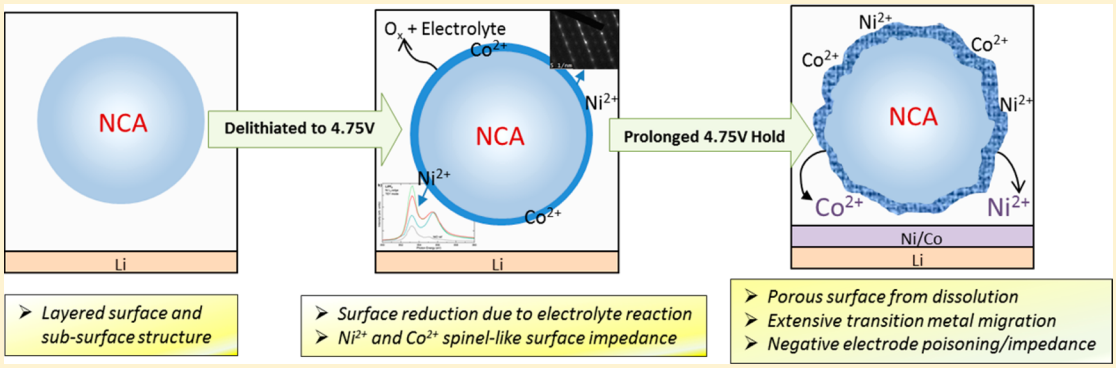

ABSTRACT: Enabling practical utilization of layered $R\bar{3}m$ positive electrodes near full delithiation requires an enhanced understanding of the complex electrode−electrolyte interactions that often induce failure. Using $Li[Ni_{0.8}Co_{0.15}Al_{0.05}]O_2$ (NCA) as a model layered compound, the chemical and structural stability in a strenuous thermal and electrochemical environment was explored. *Operando* microcalorimetry and electrochemical impedance spectroscopy identified a fingerprint for a structural decomposition and transition-metal dissolution reaction that occurs on the positive electrode at full delithiation. Surface-sensitive characterization techniques, including X-ray absorption spectroscopy and high-resolution transmission electron microscopy, measured a structural and morphological transformation of the surface and subsurface regions of NCA. Despite the bulk structural integrity being maintained, NCA surface degradation at a high state of charge induces excessive transition-metal dissolution and significant positive electrode impedance development, resulting in a rapid decrease in electrochemical performance. Additionally, the impact of electrolyte salt, positive electrode surface area, and surface Li_2CO_3 content on the magnitude and character of the dissolution reaction was studied.

INTRODUCTION

Meeting the power requirements of the next generation of portable electronics and electric vehicles will depend on significant advancements in the energy density of secondary Li ion batteries. Layered ($R\bar{3}m$) oxide cathodes materials, such as $LiCoO_2$ (LCO) and $LiNi_{0.8}Co_{0.15}Al_{0.05}O_2$ (NCA), are presently incapable of practically achieving their theoretical capacities because of an intricate and not yet fully understood combination of structural degradation and adverse cathode−electrolyte interactions that occur when approaching full delithiation. Stabilizing these materials at or near full delithiation would enable additional capacity while having a negligible impact on the cell weight and volume, resulting in increased specific and volumetric energy densities.

The initial theories for the failure of layered compounds pointed to the exfoliation of the transition-metal oxide layers of $R\bar{3}m$ compounds due to Coulombic repulsions from opposing oxygens as a result of the removal of the Li^+ ions that act as a

Special Issue: Fundamental Interfacial Science for Energy Applications

Received: March 14, 2017
Revised: May 30, 2017
Published: June 8, 2017

DOI: 10.1021/acs.langmuir.7b00863
Langmuir 2017, 33, 9333−9353

Coulombic screen. This theory was disproved approximately 20 years ago by the realization of the CdI_2 structure of fully delithiated CoO_2 and the reinsertion of over 96% of the lithium in the subsequent discharge.[1] Similar investigations revealed a degree of structural stability of NiO_2 and other layered compounds.[2] However, achieving practical reversibility of the fully delithiated structures has remained an elusive but important goal for many in the field. The challenge is complicated by the aggregate of failure modes present to various degrees among the entire $R\bar{3}m$ family. These range from electronic and/or ionic isolation induced by large lattice parameter changes resulting in electromechanical grinding to the possibility of bulk movement of the transition-metal ions to undesired surface reactions.[3−5] Surface reactions represent a primary obstacle to overcome because they are represented by a complex symbiotic interaction between the positive electrode surface and electrolyte decomposition.

Multiple studies have explored the complex interactions that these materials have with alkyl carbonate solvents and commonly used Li salts. Particularly important and the easiest to comprehend are the acid−base reactions that occur as a result of the trace levels of HF found in solutions containing $LiPF_6$ salt.[6,7] These reactions lead to the formation of electronically and ionically insulating LiF on the cathode's surface and cause transition-metal dissolution.[6−8] The acid-induced decomposition reaction produces H_2O as a byproduct, making the dissolution mechanism autocatalytic.[9] Elevated temperatures encourage the propagation of this reaction, leading to rapid structural degradation and transition-metal dissolution.[6−9] Furthermore, catalytic transition-metal oxides, especially when delithiated, can polymerize various solvents and salts, resulting in the development of a complex cathode−electrolyte interface (CEI).[10−13] X-ray photoelectron spectroscopy (XPS) and Fourier transform infrared spectroscopy (FTIR) measurements of cathode materials aged in ethylene carbonate (EC)/dimethyl carbonate (DMC) solutions containing $LiPF_6$ salt have observed a host of decomposition products, including LiF, Li_2CO_3, transition-metal fluorides, polycarbonates, P−O−F compounds, and reduced metal oxides.[10−12] For each cathode material, the composition of the CEI is dependent on the type of salt and solvent,[14,15] the presence of additives,[14,16] the temperature,[14,15,17,18] and the state of charge (SOC).[17,18] The magnitude and chemical makeup of the CEI significantly impacts the charge-transfer impedance at the cathode and can be detrimental to the cell's overall performance.[12,14,16,18]

At high states of charge, layered oxide cathode materials experience substantial structural changes in the surface and subsurface regions. When these electrodes are extensively delithiated, loss of oxygen can occur, thereby reducing transition-metal ions from the 3b sites and allowing them to diffuse to some of the vacant 3a sites, resulting in a structural transition to a disordered spinel-like ($Fd3m$) phase.[19,20] Further delithiation results in complete interlayer mixing, continued reduction of the transition metals to the bivalent state, and the release of oxygen to form a more stable rock-salt-like ($Fm3m$) structure. Because oxygen loss can be difficult in the bulk, rock-salt-like phases are generally observed on the edges of the particles.[21,22] The resulting lithium-deficient phases are responsible for increased electrical and chemical impedance on the positive electrode, which has a profound impact on the material's electrochemical performance.[23] The development of spinel and rock-salt-type phases is commonly found on or near the surface of NCA particles when subjected to extended cycling or elevated temperatures.[23−25] After only 10 cycles, NCA particles exhibit microcracking that is attributed to the volume changes during cycling, inducing greater surface exposure and subsequent reaction with the electrolyte.[26] Recently, Sallis et al. observed a large rise in impedance on NCA particles that were held at 4.5 or 4.75 V. Using TEM and XAS, they correlated the rise in impedance to the development and growth of a disordered spinel phase on the particles' surface and subsurface.[27]

During the formation of the disordered spinel and rock salt decomposition phases, the transition-metal ions are reduced to their bivalent states.[23,27] In their lower valence state, transition-metal ions are prone to dissolution, resulting in poisoning of the negative electrode, a reduced amount of electrochemically active lithium, and increased cathode impedance. During the reduction of the transition metals, extensive oxidation of the electrolyte can occur.[8,6,28] As a result of these mechanisms, a significant decline in cell performance is well documented.[29−31] Transition-metal dissolution has been shown to be highly dependent on the electrode structure, thermal environment, and electrolyte composition.[3,6,9] Additionally, it has been suggested that the electromechanical grinding that occurs in LCO during charging above 4.2 V is partially responsible for increased levels of Co dissolution.[3] Watanabe et al. observed extensive microcracking in $LiAl_{0.10}Ni_{0.76}Co_{0.14}O_2$ particles after cycling and the growth of an NiO-like layer on the new surfaces.[23] Although not directly measured, these observations support the theory that electromechanical grinding accelerates transition-metal dissolution by the creation of additional electrode interfacial area with the electrolyte. However, other mechanisms for dissolution from $R\bar{3}m$ compounds may exist and need further investigation.

Isothermal microcalorimetry has been used to measure the heat flux from electrode materials as a function of thermal,[32] electrochemical,[33−35] and compositional[36−38] conditions. In secondary lithium batteries, the heat flux during cycling is generally attributed to five sources: entropy, resistive heating, heat capacity, heat of mixing, and heat from parasitic reactions. Newman et al. developed a thorough model for heat-generation sources in an insertion battery[39,40] and then later published extensive work on the heats of mixing and entropic heating.[41,42] Other literature has focused on the multiple sources of irreversible heating[43] and heat production as a function of the state of charge.[33−36,44,45] The heat generation during charge and discharge has been measured for a variety of positive electrode chemistries including $LiCoO_2$-,[33,35,46] $LiFePO_4$-,[32,47] $LiNi_{0.8}Co_{0.15}Al_{0.05}O_2$-,[33,48] and $Li[Ni_xMn_yCo_z]O_2$-type[36,38,49] materials. Although much of the published battery research utilizing isothermal microcalorimetry is focused on the entropic and resistive heating during cycling, publications by Dahn et al. have isolated the thermal contribution from parasitic reactions and provided a quantitative measurement of the cathode−electrolyte reactions that occur at high states of charge.[38,50−55] By exploiting the different relationships between the sources of heat and the current, Dahn et al. were able to attribute the heat flow to entropy, polarization, or parasitic side reactions. Their work focused on the heat flow over small potential windows at potentials above 4.2 V and investigated the role that different electrolytes and electrolyte additives have on the parasitic reactions.[38,50,51,54,55]

The focus of this work is the stability of NCA at full delithiation, under constant potential (4.75 V) and at elevated

DOI: 10.1021/acs.langmuir.7b00863
Langmuir 2017, 33, 9333−9353

temperature (60 °C), to investigate the relationship between the electrode and electrolyte as well as the modifications of the surface and subsurface structures of NCA. This protocol was performed without cycling to prevent extensive microcracking, which may induce a significant increase in the electrode−electrolyte interfacial area. These conditions represent the most stressful, practical environment for evaluating such materials in order to understand the driving force toward failure at full delithiation without going to such extremes that would activate new failure modes. Although such conditions seem extreme for carbonate electrolytes, especially using $LiPF_6$, it has been shown that carbonate electrolytes enable excellent reversibility for 500 cycles in high-voltage spinels at 60 °C with a charge cutoff of 4.99 V.[56,57] The high degree of reversibility is stable as long as the electrode material does not induce a significant decomposition reaction with the electrolyte.

Continuous measurement of the parasitic reactions on NCA cathodes was achieved through *Operando* isothermal microcalorimetry and electrochemical impedance spectroscopy (EIS). These techniques enabled the determination of the magnitude and character of the parasitic reactions as a function of voltage, temperature, and electrolyte salt. Surface-sensitive characterization methods, such as high-resolution transmission electron microscopy (HRTEM) and X-ray absorption spectroscopy (XAS), were employed to observe the structural and compositional changes occurring at the material's surface. Coupling these techniques with dissolution measurements obtained by energy-dispersive spectroscopy (EDS) and inductively coupled plasma−atomic emission spectroscopy (ICP−AES) facilitated a deeper understanding of the impact that parasitic reactions have on the structural stability of NCA and the overall performance of the cell.

EXPERIMENTAL SECTION

Preparation of Materials. $LiCoO_2$ (Seimi) and $LiNi_{0.8}Co_{0.15}Al_{0.05}O_2$ (NAT1050, TODA America) were mainly used as received, and electrodes were made using the Bellcore method.[58] Electrode tapes were cast in a dry room (<1% relative humidity) to minimize their exposure to moisture. Casting slurries were a mixture of poly(vinylidene fluoride-*co*-hexafluoropropylene) (PVDF-HFP, Kynar 2801, Elf Atochem), carbon black (Super P (SP), MMM), propylene carbonate (Aldrich), and acetone (Aldrich). Homogenous slurries were cast and allowed to air dry, and then the propylene carbonate plasticizer was extracted by soaking the tape in 99.8% anhydrous diethyl ether (Aldrich). Electrodes with a composition of 88.81 wt % active material, 3.91 wt % SP, and 7.28 wt % PVDF-HFP were used unless otherwise specified. To accommodate the higher surface area and Li_2CO_3 samples, an electrode composition of 79.87 wt % active, 7.03 wt % SP, and 13.10 wt % PVDF-HFP was utilized. The free-standing tapes were subsequently dried at 120 °C under vacuum for a minimum of 10 h and stored in an Ar-filled glovebox to avoid atmospheric exposure. High-surface-area NCA was achieved by high-energy milling of the pristine material for 15 min at 400 rpm (Retsch PM100). Milling samples were prepared in an Ar-filled glovebox, where the dried powder was sealed in a zirconium oxide-lined milling cell. After milling, the cell was returned to the glovebox so that the sample could be retrieved with no exposure to the ambient atmosphere. To prepare NCA samples with increased Li_2CO_3 content, samples were deliberately exposed to ambient air for 2 weeks by resting in a hood with constant air flow.

Electrochemical Characterization. Coin cells (2032, Hohsen) and three-electrode cells (in-house) were assembled in an Ar atmosphere glovebox using Whatman GF/D glass fiber separators saturated with either a 1 M $LiPF_6$ or 1 M $LiBF_4$ ethylene carbonate/dimethyl carbonate (EC/DMC) (1:1 volume ratio) solution (BASF) (<20 ppm of H_2O) and a lithium metal (FMC) negative electrode. To eliminate the signal interference and possible interactions caused by the PVDF-HFP binder, powder cells composed of 97.5 wt % active material and 2.5 wt % carbon black were used for all XAS, XPS, and HRTEM measurements. Powder cell fabrication was identical to that of cells with tape electrodes except that in addition to the glass fiber separator, PVdF-HFP-based and polyolefin (Celgard) separators were used. Potentiostatic and galvanostatic electrochemical testing was controlled by a VMP3 (Biologic) or Maccor battery cycling system at either 24 or 60 °C. Cells were galvanostatically charged at 25 mA/g of active material (~C/11) to V_{max} (4.1, 4.5, or 4.75 V), held under potentiostatic conditions for varying amounts of time, and then discharged at 5 mA/g (~C/55) to 2.7 V. Electrochemical impedance spectroscopy (EIS) scans were carried out using the VMP3, with a frequency range of 400 kHz to 15 mHz and a 20 mV sinusoidal amplitude. EIS scans were performed under open circuit conditions unless the cell was in a potentiostatic hold, in which case the sinusoidal amplitude was added on top of the potentiostatic potential.

Physical Characterization. Thermogravimetric analyses (TGA) were performed by utilizing Pt pans in a TA Instruments TGA 2050. Experiments were performed by heating at 5 °C/min to 600 °C and then holding at 600 °C for 5 h. Flowing dry air was used throughout the entire test. Multipoint Brunauer−Emmett−Teller (BET) surface-area experiments were conducted on a Micromeritics ASAP 2020 analyzer using N_2 gas. Samples were degassed under vacuum at 120 °C for at least 20 h prior to evaluation.

ICP−AES analysis was completed by Galbraith Laboratories, Inc. (Knoxville, TN). ICP−AES samples were prepared by dissolving Li negative electrodes in 37 vol % HCl and adding DI water until the total volume was 7 mL. All cells for ICP−AES testing were assembled using additional Cu current collectors to prevent transition-metal contamination from the stainless steel cell body. The average sample mass was 7.444 g, with all samples having a mass within 1.55% of the mean. The total amounts of Co and Ni dissolution were calculated by extrapolating the measured concentration to the entire sample mass. The percentage of dissolved Co and Ni was determined by dividing the mass of the measured dissolution products by the initial amount of Co and Ni present in each sample. Field-emission scanning electron microscopy (FESEM) results were obtained on a Zeiss microscope, and energy-dispersive X-ray spectroscopy (EDS) data was obtained with an INCAPenta FETx3 detector (Oxford Instruments). Samples were exposed to the ambient atmosphere for about 1 min during sample transfer into the microscope.

The transmission electron microscopy experiments were performed using a JEOL 2010F microscope operated at 197 kV. The spatial resolution of the microscope in the high-resolution (HRTEM) mode is ~1.4 Å. The fast Fourier transform (FFT) of the HRTEM images generates spots that correspond to crystallographic periodic arrangements of atomic planes. These spots were also used as filters to remove background noise from the high-resolution images. The filtered HRTEM images provide crystallographic information from an approximate area of 16 nm^2. The smallest selected-area aperture was used to obtain diffraction from an area within the first 100 nm of the edge of the particle. All HRTEM and selected-area electron diffraction (SAED) patterns were analyzed using a Gatan Digital Micrograph. In addition, the experimental SAED patterns were indexed using JEMS software.

A Bruker D8 Advance diffratometer (Cu Kα, λ = 1.5406 Å) was used for all X-ray diffraction (XRD) characterization. XRD analysis of cycled electrodes was conducted by disassembling and retrieving the sample electrode in an Ar-filled glovebox. The electrode was then washed with DMC to remove any residual electrolyte and allowed to dry in the glovebox. To minimize atmospheric exposure, the dried samples were sealed onto glass slides using Kapton film and X-ray-transparent grease, prior to leaving the glovebox. XRD scans were conducted over a 2θ range of 15−70° at a scan rate of about 0.6°/min.

For all XPS spectroscopy measurements, disassembled NCA powder electrodes were mounted on conductive tape and transferred using vacuum suitcase setups between the glovebox and vacuum chamber to avoid any exposure to air. XPS measurements were performed using a Phi VersaProbe 5000 system at the Analytical and

DOI: 10.1021/acs.langmuir.7b00863
Langmuir 2017, 33, 9333−9353

Diagnostics Laboratory (ADL), Binghamton University. A flood gun was used to charge compensate insulating samples, and the carbon black C 1s peak was aligned to 284.5 eV to account for possible charging effects.

Soft XAS was performed at beamline I09 at Diamond Light Source Ltd. (DLS) and beamline 8.0.1 at the Advanced Light Source (ALS) at the Lawrence Berkeley National Laboratory (LBNL). At both facilities, a vacuum suitcase setup was employed to avoid any surface contamination. X-ray absorption spectroscopy in the surface-sensitive total electron yield (TEY) was conducted at both beamlines. Additional bulk-sensitive partial fluorescence yield (PFY) modes were used at beamline 8.0.1 at the ALS. Measurements were repeated at both facilities whenever possible and were highly reproducible. All spectra were normalized to the current from a reference Au-coated mesh in the incident photon beam. The energy resolution was close to 0.1 eV (I09) and 0.2 eV (8.0.1) at the O K-edge. For the O K-edge, TiO_2 was used to calibrate the photon energy axis. Ni metal was used to calibrate the photon energy axis for the Ni L-edge.

***Operando* Microcalorimetry.** An MMC 274 Nexus multimode calorimeter with a high-temperature coin cell module (Netzsch) was utilized to perform isothermal microcalorimetry and differential scanning calorimetry experiments in parallel with electrochemistry. Samples were standard 2032 coin cells (previously described) oriented with the positive electrode flush against the sample heat flux sensor. To eliminate the thermal contribution from heat sources other than the electrodes, a reference cell consisting of all stainless steel cell parts, the separator, and the electrolyte was used. The reference cell was placed on the reference heat sensor, which is located directly opposite the sample sensor. The measured heat flux is the difference in the heat flux between the sample and reference sensors. For all microcalorimetry experiments, the thermal protocol is as follows: heat to 30 °C at 0.5 °C/min, isothermal at 30 °C for 20 h, heat to 45 °C at 0.5 °C/min, isothermal at 45 °C for 20 h, heat to 60 °C at 0.5 °C/min, and a final isothermal step at 60 °C until the end of the experiment.

RESULTS AND DISCUSSION

Reaction Identification. NCA half-cells were charged at 25 mA/g to 4.1, 4.5, or 4.75 V at 60 °C and then held at constant voltage, as shown in Figure 1. After being charged at constant current, cells with a 4.1 or 4.5 V cutoff showed a current decay to near 0 mA/g within 20 or 30 h, respectively, as a result of the delithiation reaction reaching equilibrium. This current eventually relaxes into a steady state leakage current, which remains constant for the remainder of the experiment. The NCA cell with a 4.75 V cutoff also has a relaxation current at the beginning of the potentiostatic segment related to the completion of the delithiation reaction. Afterward the current plateaus to a much higher corrosion current than for the analogous 4.5 V cell (1.495 mA/g vs 0.100 mA/g). In contrast to the cells at 4.1 or 4.5 V, the current of the 4.75 V cell begins to increase after approximately 30 h at constant voltage and ultimately reaches a peak of around 10 mA/g. After peaking, a large decay in current is observed, and the current plateaus to a steady state rate. Because the potential of the negative electrode is independent of the cell's SOC and the parasitic reactions were observed only at 4.75 V, the measured peak in current is not due to a thermally induced reduction of the electrolyte at the Li negative electrode. Any negative electrode interaction with electrolyte would be independent of the charge voltage. The elevated current is observed only at 4.75 V, so highly delithiated NCA must be necessary for the reaction to occur.

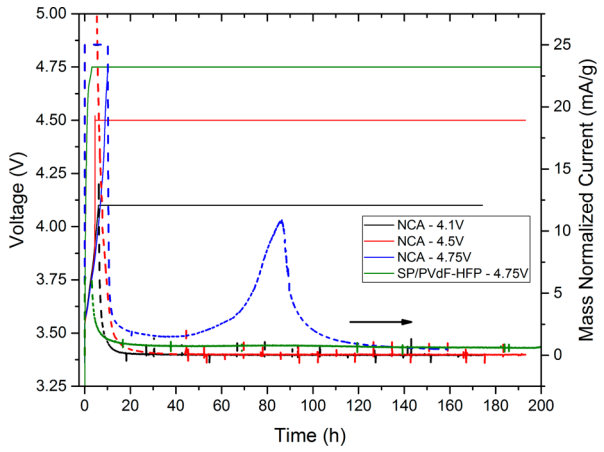

Figure 1. Voltage and current profiles as a function of time for NCA and SP/PVdF-HFP half-cells that were charged to and held at the upper cutoff potential while at 60 °C. The upper cutoff potential was either 4.1, 4.5, or 4.75 V. Voltage data and current data are scaled according to the left and right axes, respectively.

All NCA electrodes shown in Figure 1 consist of 3.91 wt % SP to improve the electrical conductivity. To identify any interactions between the SP and the electrolyte in this aggressive electrochemical and thermal environment, an electrode composed of only SP (20 wt %) and PVdF-HFP was tested under identical conditions. Because the SP/PVdF-HFP cell has no active material, a 20 μA charging current was used, and the mass-normalized current data presented in Figure 1 (green) is based on the amount of SP. The SP/PVdF-HFP positive electrode has no peak in current, signifying that the peak in current experienced in the 4.75 V NCA cell is a result of cathode−electrolyte interactions and not simply the oxidation of the electrolyte. Additionally, despite having nearly 1.81 times the absolute amount of SP that the 4.75 V NCA electrode has, the SP/PVdF-HFP electrode did not show an increased leakage current at 4.75 V, indicating that the SP is not a catalyst for the increased current.

Operando microcalorimetry enables the continuous monitoring of the heat flux and current as well as intermittent impedance measurements while providing control of the cell's electrochemical and thermal conditions. To validate our microcalorimetry setup and also provide a contrast to NCA, LCO electrodes were initially characterized. Figure S1 presents the heat flux (black), voltage (green), and current (blue) data from an *Operando* microcalorimetry experiment on an LCO positive electrode as it was charged to 4.75 V and held potentiostatically while under isothermal 30 °C conditions. After the 4 h open circuit voltage (OCV) period, which allows the chamber temperature and heat flux signal to fully stabilize, the half-cell was charged at a constant current of 25 mA/g (~C/11). Relative to the stable background heat flux taken at the end of the OCV period, the initial delithiation reaction is endothermic and remains endothermic until the cell potential is slightly greater than 4 V. Between ~4.08 and 4.28 V, a significant exothermic peak is observed, which correlates to the hexagonal to monoclinic Li ordering phase transition. Immediately following this peak is a second less-intense peak, which starts at about 9.25 h and is associated with the structural transition back to the hexagonal phase. As the LCO electrode approaches full delithiation, the delithiation reaction becomes very exothermic. The heat flux profiles for the LCO electrode during charging are consistent with the results from Saito et al.,[33] Kobayashi et al.,[59] and Miyashiro et al.[46] and validate our experimental setup. Once within the 4.75 V constant voltage hold, the current and exothermic heat flux relax as the electrode approaches the equilibrium Li^+ concentration.

DOI: 10.1021/acs.langmuir.7b00863
Langmuir 2017, 33, 9333−9353

To investigate the interesting peak in corrosion current shown in Figure 1 and contrast the results with LCO, LCO and NCA half-cells were charged to 4.75 V and held under potentiostatic conditions in the microcalorimeter. Additionally, the effect of temperature was explored by changing the thermal environment throughout the experiment. The thermal profile for all microcalorimetry experiments was as follows: after 20 h at 30 °C the temperature was increased to 45 °C, held isothermally for an additional 20 h, and then increased to 60 °C, where it remained until the conclusion of the experiment. While at 4.75 V and 60 °C, the duplicate *Operando* microcalorimetry cells, in Figure 2 and Figure S2, show a

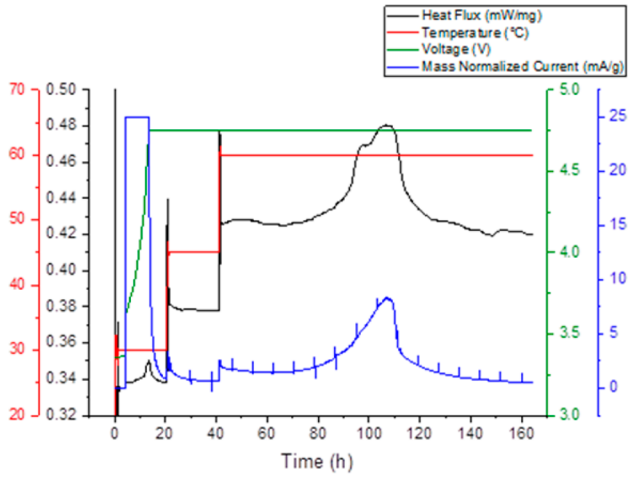

Figure 2. Heat flux (black) and electrochemical (blue and green) measurements from an *Operando* microcalorimetry experiment on an NCA half-cell as it was charged to and held at 4.75 V. The NCA cell was held at constant potential while the temperature (red) was incrementally stepped up from 30 to 45 to 60 °C.

peak in the current data nearly identical to the current response shown for the nonmicrocalorimetry NCA cell at 4.75 V in Figure 1. A large peak in the heat flux mirrors the current, indicating that the parasitic reactions are highly exothermic. The data in Figure S3 is of an LCO half-cell, and the results in Figure 2 and Figure S2 are of duplicate NCA half-cells. All of the cells were tested under identical conditions, which demonstrates that the measurement of parasitic reactions is highly reproducible, as is the duality between the heat flux and current profiles. The exothermic reactions shown in Figures S2 and S3 and Figure 2 are either self-passivating or become exhausted because the magnitude of both the heat flux and current at the end of the test are similar to their values at the beginning of the 60 °C phase. The measurement of the parasitic exotherm in LCO and NCA is significant because it discredits the notion that the reactions are intrinsic to either material and instead indicates that the parasitic reactions are correlated to the $R\bar{3}m$ structure or possibly the transition metals themselves.

Clearly, the LCO half-cell initiates the current rise much earlier than does NCA. Parasitic reactions were induced as soon as the LCO half-cell was heated to 60 °C, whereas NCA required nearly 30 h at 60 °C before the onset of the current peak. Using the final heat flux as a baseline, at 60 °C the LCO cell in Figure S3 had a cumulative heat of 11487.8 J per gram of active material (J/g). Similar analysis of the NCA cells in Figures 2 and S2 determined that the cumulative heats were 6527.7 and 7004.9 J/g, respectively, about half of the heat produced by the LCO cell. The higher instability of LCO relative to NCA is in agreement with other thermal studies.[17,60] A corresponding microcalorimetry evaluation using an electrode without the $R\bar{3}m$ positive electrode material but with all other components (SP, PVDF-HFP, etc.) did not show an evolution in current or an exotherm at 4.75 V and 60 °C consistent with the response in current already shown in Figure 1.

Selected impedance scans extracted from the NCA microcalorimetry test shown in Figure S2 are presented in Figure S4a,b. Figure S4a shows the holistic view encompassing all of the Nyquist data, and Figure S4b portrays the same data but focuses on the lower impedance region. The initial impedance scan at 4.75 V (black data), taken at 14 h, has a two-semicircle shape with a total impedance of <70 Ω. As the NCA electrode continues to delithiate during the 30 and 45 °C segments, the semicircle associated with the charge-transfer impedance grows. The impedance scan taken at 62 h (blue data) shows that prior to the exothermic reactions the total cell impedance is relatively small but has still increased by almost 1300 Ω. As the parasitic reactions begin to occur, the impedance growth is rapidly accelerated. Total impedance of the EIS scan taken near the peak of the exotherm (110 h, green data) is around 2 orders of magnitude larger than the pre-exotherm scan (62 h, blue data) as a result of impedance growth. Although the parasitic reactions fade out, the large increase in charge-transfer impedance continues such that at the end of the test the total impedance is about 3 orders of magnitude greater than the pre-exotherm levels.

Besides the parallel evolution of a heat exotherm and a peak in the current, two other characteristics are of specific importance: (i) the massive increase in cell impedance and (ii) the low OCV of approximately 2.5−3 V of the post-exotherm cells. Considering that the NCA is near full delithiation, the low OCV could have been a result of the complete decomposition of the layered oxide into a spinel or rock-salt-type structure. At first glance, this seems to be the likely scenario. To investigate the plausibility of this reaction mechanism, after the microcalorimetry experiment the coin cell was disassembled in a glovebox and evaluated by ex situ XRD. The XRD scans displayed in Figure 3 show that the initial

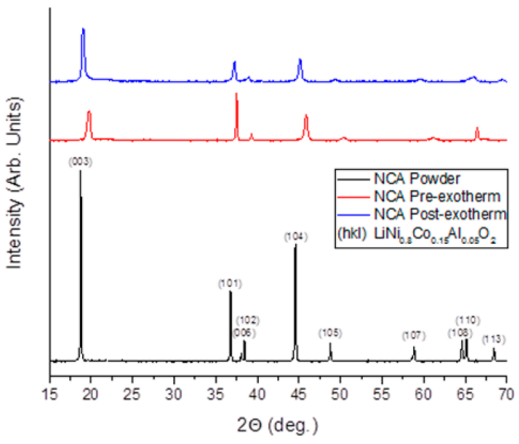

Figure 3. Comparison of XRD results of the pristine powder (black) and the positive electrodes before (red) and after (blue) exothermic reactions at 4.75 V and 60 °C for NCA. The peaks associated with the layered ($R\bar{3}m$) structure are indexed for the pristine material.

DOI: 10.1021/acs.langmuir.7b00863
Langmuir 2017, 33, 9333−9353

rhombohedral layered structure (referred to as O3) is retained in the pre-exotherm and post-exotherm NCA samples and exhibits good preservation of the (003)/(104) ratio and (108)/(110) peak splitting. These results are indicative of little transition-metal movement to the Li 3a sites, which would have been observed in a bulk transformation to spinel/rock salt structures. Minor Bragg peak shifts are associated with variations in Li content as post-exotherm cells do not relithiate completely. Although the relative intensity of the post-exotherm NCA sample is lower than that of the pristine or pre-exotherm samples, a close evaluation of the data shows no new peaks or phases, suggesting no significant amount of oxygen loss. In contrast to NCA, post-exotherm LCO, presented in Figure S5, shows a structural transformation of the rhombohedral layered phase to a hybrid phase of the initial rhombohedral and a hexagonal CoO_2 structure (referred to as H1-3). This is the layered phase that is expected to develop at high degrees of delithiation for LCO and again represents no significant oxygen loss or bulk decomposition.[61] The transformation and retention of the crystalline O1 CoO_2 phase is highly dependent on the removal of all Li^+ ions. In summary, no evidence of bulk oxygen loss or subsequent decomposition of either the NCA or LCO phase can be attributed to the exotherm or the low OCV after reaction.

During the disassembly of the microcalorimetry cells, visual observation noted the extreme deposition of transition-metal dissolution products on the negative electrode. EDS was utilized to detect the presence and determine the relative magnitude of the transition-metal plating on the Li negative electrodes. Figure S6 shows FESEM and EDS mapping images of Li negative electrodes extracted from NCA coin cells before and after exothermic reactions. Ni and Co EDS measurement results are shown in Figure S6b,c for the pre-exotherm sample and in Figure S6e,f for the post-exotherm sample. In each sample, the left side of the negative electrode was thoroughly scraped to remove any products that either formed or were deposited on the surface. Because the long-range diffusion of Ni or Co into the Li metal is assumed to be negligible, removing all surface products creates an internal reference that can be used to estimate the magnitude of transition-metal deposition. The Li negative electrodes are on stainless steel substrates, so there are trace amounts of detectable Ni and Co even in the absence of any dissolution products. The pre-exotherm sample shows that prior to the exothermic peak there is definitely some Ni and Co deposition on the untouched negative electrode relative to the scraped area. In contrast, after exothermic reactions very high concentrations of Ni and Co metal are measured. Normalized to the cleaned areas, the post-exotherm negative electrode has between a 5- and 7-fold increase in both the Ni and Co concentrations.

XRD (Figure 4) of a Li negative electrode after a microcalorimetry experiment revealed that at least a portion of the Ni and Co deposition products are fully reduced to their metallic structures. In Figure 4, the Li, Ni, and Co metal Bragg reflections are denoted by black circles, red diamonds, and blue asterisks, respectively. As expected from using a Li foil negative electrode, the Li metal peaks are strong and narrow and the Ni and Co peaks are very broad as a result of their likely nanosized domains.

The reassembly of multiple post-exotherm cells with fresh negative electrodes and electrolyte reveals that the OCV of the positive electrode is reproducibly between 4.1 and 4.3 V, indicative of a delithiated positive electrode. This suggests that

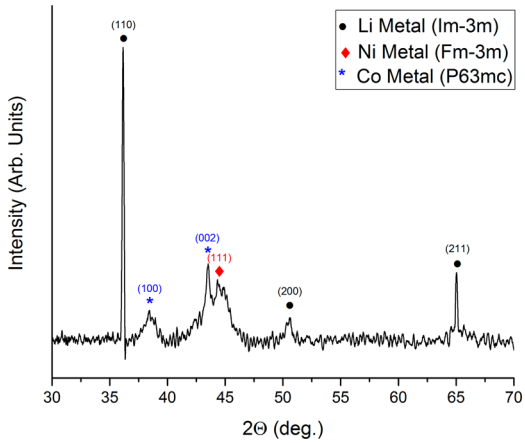

Figure 4. XRD plot of a Li foil negative electrode retrieved from an NCA microcalorimetry cell after testing at 4.75 V and 60 °C. The main Li, Ni, and Co metal peak locations are marked by a black circle, red diamond, and blue asterisk, respectively. For each phase, the main peaks are indexed according to the listed space groups.

the low OCV voltage of 2.5−3 V observed in the initial cell was a result of a potential shift induced at the negative electrode, possibly due to the dissolution products from the positive electrode. The reassembled cells also showed a total impedance that was orders of magnitude smaller than for the post-exotherm cell, proving that the negative electrode was the origin of such an increase. However, it should be noted that the post-exotherm cells still exhibited a positive electrode impedance that was approximately an order of magnitude greater than for the original cell. This suggests that some degree of degradation of the positive electrode did occur but could not be rectified with immersion in fresh electrolyte and a new negative electrode. Such surface transformations will be discussed in a later section of this article. Subsequent discharge of the reassembled cells revealed that a specific capacity in the range of 119−145 mA h/g could be achieved as opposed to no specific discharge capacity before the cell was reassembled.

Three-Electrode Electrochemical Analysis. Particularly peculiar was the observation that the dissolution products induced a significant shift in the post-exotherm cell OCV to the very low voltage of 2.5−3 V, as noted above. To distinguish between the changes occurring on the positive and negative electrodes during the exothermic reaction, a three-electrode cell was constructed and tested under similar electrochemical and thermal conditions to those present in the microcalorimetry characterization. The three-electrode cell, shown in Figure 5a, is composed of NCA positive, Li metal negative, and Ag metal quasi-reference electrodes. Reference electrode materials were chosen so that they would not reduce the transition-metal dissolution products present in the electrolyte. Obviously, a Li reference electrode would not be effective, and results (not shown) using $Li_4Ti_5O_{12}$ as the reference electrode also showed reactions with the dissolution products. Thus, Ag and V_2O_5 were chosen as suitable quasi-reference and reference electrode materials, respectively.

Analogous to the microcalorimetry tests displayed in Figure 2 and Figure S2, the results of a three-electrode experiment are shown in Figure 5a. Unlike the microcalorimetry experiments that had a varying temperature profile, the three-electrode cells were in a 60 °C incubator for the entirety of the test. In contrast to the two-electrode arrangement of the microcalorimetry cell, the three-electrode cell also includes a Ag

DOI: 10.1021/acs.langmuir.7b00863
Langmuir 2017, 33, 9333−9353

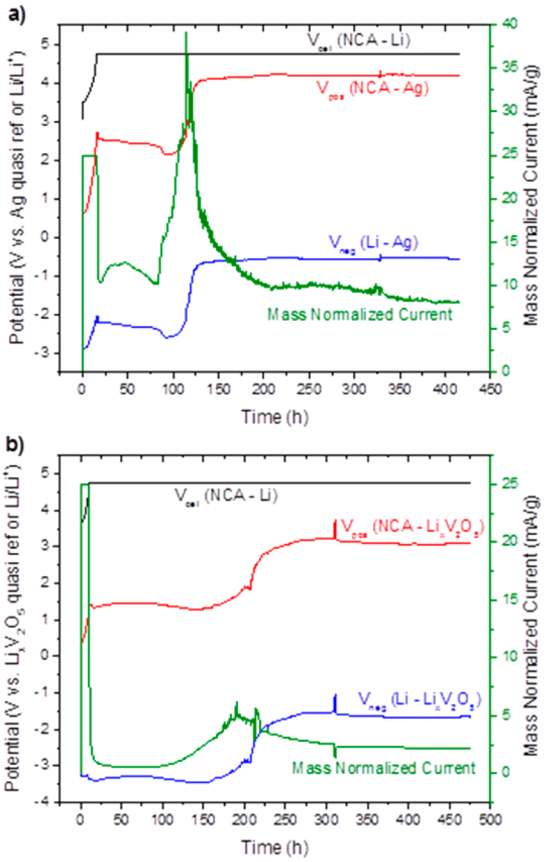

Figure 5. Three-electrode electrochemical cells with an NCA positive, Li metal negative, and (a) Ag metal quasi-reference or (b) $Li_xV_2O_5$ reference electrode. The cell potential was charged to 4.75 V (vs the Li negative electrode) at 25 mA/g and then held at 4.75 V at 60 °C. The positive and negative electrode potentials are each relative to the reference electrode, and the cell potential is the difference between the positive and negative electrodes. The cell (black), positive (red), and negative (blue) potentials are scaled according to the left axis, and the current (green) is correlated with the right axis. The three-electrode cells in panels (a) and (b) were identically made, except for the reference electrode used.

metal quasi-reference electrode that enables the simultaneous and objective measurement of the positive and negative electrode potentials. The two-electrode output voltage of $V_{pos} - V_{neg}$ represented by V_{cell} is similar to the microcalorimetry cell in Figure 2. The cell voltage is raised to 4.75 V versus Li/Li^+ during the complete delithiation of NCA followed by a featureless constant voltage hold at 4.75 V versus V_{neg} for approximately 400 h. The evolution of the current is also in agreement with the two-electrode microcalorimetry experiments. Specifically, after approximately 83 h at 4.75 V a large increase in current is observed, which peaks and then dissipates. In the microcalorimetry evaluation, this peak in current parallels the evolution of the exotherm. What is surprising is the evolution of the positive and negative electrode potentials relative to the reference electrode. Approximately 20 h after the initiation of the parasitic current spike, a significant rise in the potentials of the negative and positive electrodes was observed, paralleling a rapid increase in current. Within the next 50 h, the potentials of the positive and negative electrodes increase by ~2 V relative to the reference electrode and the parasitic current starts to decline as the reactions appear to be nearing completion. The adjusted potential of the negative electrode is consistent with the redox potential of Ni and Co. For the remainder of the potentiostatic phase, the parasitic current continues to taper off, and the electrode potentials stabilize.

The evidence presented within the three-electrode analysis suggests that after a period of time at 4.75 V versus V_{neg} a corrosion reaction commences, resulting in the rapid dissolution of the positive electrode surface into the electrolyte. The dissolution reaction products migrate and deposit on the negative electrode, inducing a large potential shift of the negative electrode due to the formation of a mixed potential of Li with deposited transition metals. Because the experiment is run at constant potential (4.75 V vs Li negative electrode), the positive electrode potential is raised to maintain the Δ of 4.75 V between the positive and negative electrodes. This translates to the NCA electrode rising above 6 V versus Li/Li^+ (likely greater than 7 V), undoubtedly further accelerating the dissolution of the positive electrode. As the mixed potential of the negative electrode becomes weighted toward the metal products, the potential shift continues to increase. One can envision this entire experiment as an accelerating rate study of an electrode material's tendency to form dissolution products. The reaction eventually ceases and the current is lowered to a constant corrosion state when either the positive electrode becomes passivated or the impedance at the negative electrode becomes so large that it cannot support the electrochemical oxidation reaction at the positive electrode.

Because quasi-reference electrodes can be prone to a shift in potential, the three-electrode results were validated by cross checking these interesting observations with a three-electrode configuration consisting of a more stable intercalation-based reference electrode. In addition to being stable, the redox potential of $Li_xV_2O_5$ is also higher than the standard reduction potentials of both Ni and Co, thus preventing Ni and Co dissolution products from poisoning the $Li_xV_2O_5$ reference electrode. Figure 5b displays the electrode potentials and the mass-normalized current for this cell, which was tested identically to the first three-electrode cell. As with the Ag metal reference, the potential of the $Li_xV_2O_5$ electrode drifts slightly during charging, and its equilibrium potential was assumed to be 3.46 V versus Li/Li^+, which corresponds to the potential of V_{neg} at around 140 h. At the beginning of the potentiostatic phase, the gradual current relaxation is due to the extraction of the remaining Li ions from the cathode. With time, the relaxation current transitions into a stable leakage current, and the potentials of both electrodes are little changed. Starting around the 100 h mark, the current rises in accordance with the beginning of the parasitic reactions. Similar to the three-electrode cell in Figure 5a, there is a delay before an increase in the potentials of the positive and negative electrodes versus the $Li_xV_2O_5$ reference. Once the electrode potentials do begin to change, they quickly experience an ~2 V adjustment versus the reference electrode, comparable to the potential shift shown in Figure 5a. While the working and counter electrode potentials are adjusting, the parasitic current decreases in intensity and eventually plateaus as the electrode potentials steady. Figure S7 displays the corresponding impedance data taken at the beginning (solid lines) and the end (dashed lines) of the experiment. Initial scans show little impedance between the positive and reference electrodes, negative and reference electrodes, and positive and negative electrodes. EIS data taken at the conclusion of the test measure little change in the positive electrode impedance but an order of magnitude increase in the negative electrode.

DOI: 10.1021/acs.langmuir.7b00863
Langmuir 2017, 33, 9333−9353

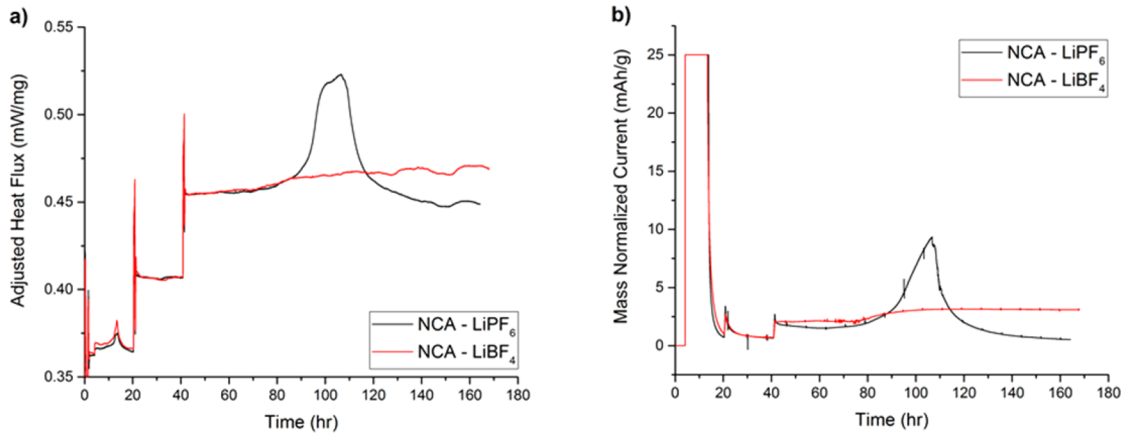

Figure 6. (a) Heat flux and (b) current profiles for microcalorimetry experiments of NCA half-cells made with 1 M $LiPF_6$ (black) and 1 M $LiBF_4$ (red) salt in EC/DMC (1:1) solvent. Cells were charged to 4.75 V at 25 mA/g and held potentiostatically while the temperature of the microcalorimeter was changed from 30 to 45 to 60 °C.

The potential, current, and impedance data for a third three-electrode cell, made similarly to the one presented in Figure 5b, is shown in Figures S8 and S9. Despite being tested identically to the other three-electrode cells, this cell does not show a large peak in the parasitic current or a shift in the counter electrode potential. This is undoubtedly due to the fact that the dissolution products did not diffuse to the negative electrode and react in such excess that would result in a potential shift, thereby initiating the accelerating rate dissolution reaction. It should be noted that the physical architecture of the three-electrode cell is different and much more tortuous than that of the coin cell, the latter of which has and will be further shown to offer very reproducible results. However, the initial development of the parasitic current as represented by a small peak in current is indistinguishable from that of the other three-electrode cells, suggesting that the transition metals entered the electrolyte via this prereaction but were never deposited on the negative electrode, resulting in a potential shift. We have observed this result in a fourth three-electrode cell with construction similar to that of the cell in Figure 5a. This result is important because it shows the intrinsic current development from the parasitic reactions initially induces the transition-metal dissolution at the NCA surface. It does so without having any artifacts in the current response directly associated with the current needed to raise the cell potential or the current evolved from the positive electrode at potentials in excess of 4.75 V versus Li/Li^+. This mirrors behavior in a shoulder identified in the exotherm of Figure S2. Figure S9 displays the EIS data taken at the beginning and the end of the experiment. In contrast to the previous cells, there is little impedance growth on the negative electrode but a 2 orders of magnitude increase on the positive electrode. The lack of significant impedance development on the negative electrode supports the conclusion that a majority of the transition-metal ions in the electrolyte were not able to deposit on the negative electrode.

Impact of Electrolyte Salt on Heat Flux and Impedance. The impact of the electrolyte salt composition on the exothermic reactions was studied by performing identical microcalorimetry experiments on NCA electrodes using 1 M $LiPF_6$ EC/DMC (1:1) and 1 M $LiBF_4$ EC/DMC (1:1). The comparisons of the heat flux and current profiles for the two electrolytes are shown in Figure 6a,b, respectively. Both electrolytes show nearly identical heat fluxes and current profiles during the 30 °C, 45 °C, and pre-exotherm 60 °C segments. This indicates that very little differences in corrosion behavior beyond the effects of the solvent are active in these regions. In contrast to the exothermic reactions that occur with $LiPF_6$ salt at 4.75 V and 60 °C, samples with $LiBF_4$ have a moderate increase in both heat flux and current and maintain this elevated state until the cell vents without the formation of a sharp exotherm.

Selected scans from the corresponding *Operando* impedance measurements for the $LiPF_6$ and $LiBF_4$ microcalorimetry samples are displayed in Figure S10a,b, respectively. As previously mentioned, the exothermic reaction enabled by $LiPF_6$ salt causes a drastic impedance development; however, samples utilizing $LiBF_4$ have only a modest impedance rise that directly correlates to the growth of the current. From each EIS scan, three key impedance values were extracted. The electrical resistance of the cell (mainly from electrolyte) is denoted as R1. The impedance of the solid−electrolyte interface on the negative electrode is represented by R2, and the impedance of the cathode and cathode−electrolyte interface is recorded as R3. For clarity, Figure S10b contains a visual example of the three fitted impedance values for the 229 h Nyquist plot. A direct comparison of all of the impedance values obtained from the EIS data sets shown in Figure S10a,b is presented in Figure 7a−c. When interpreting the data, it is important to be cognizant of the temperature change from 30 to 45 °C after 20 h and the increase from 45 to 60 °C at around 40 h. For both salts, the R1 impedance (Figure 7a) is relatively small and stable throughout the experiment. As expected from the increase in the conductivity of the electrolyte, the R1 impedance drops as the cells are heated from 45 to 60 °C, followed by a slow, gradual increase as the cells are held at 4.75 V and 60 °C.

Unlike the R1 data, which shows little difference between the two salts, the impedance of the solid−electrolyte interface of the negative electrode (R2) presented in Figure 7b has a stark distinction. For the $LiPF_6$ sample, the R2 impedance slowly begins to increase after the scan taken at 38 h. The rate of impedance growth accelerates after the 70 h scan, which correlates to the development of parasitic heat and current shown in Figure 6a,b, respectively. Following the 102 h scan, a large impedance development is observed and results in the R2 impedance increasing by over 2 orders of magnitude. The exponential rise in impedance begins as the parasitic current

DOI: 10.1021/acs.langmuir.7b00863
Langmuir 2017, 33, 9333−9353

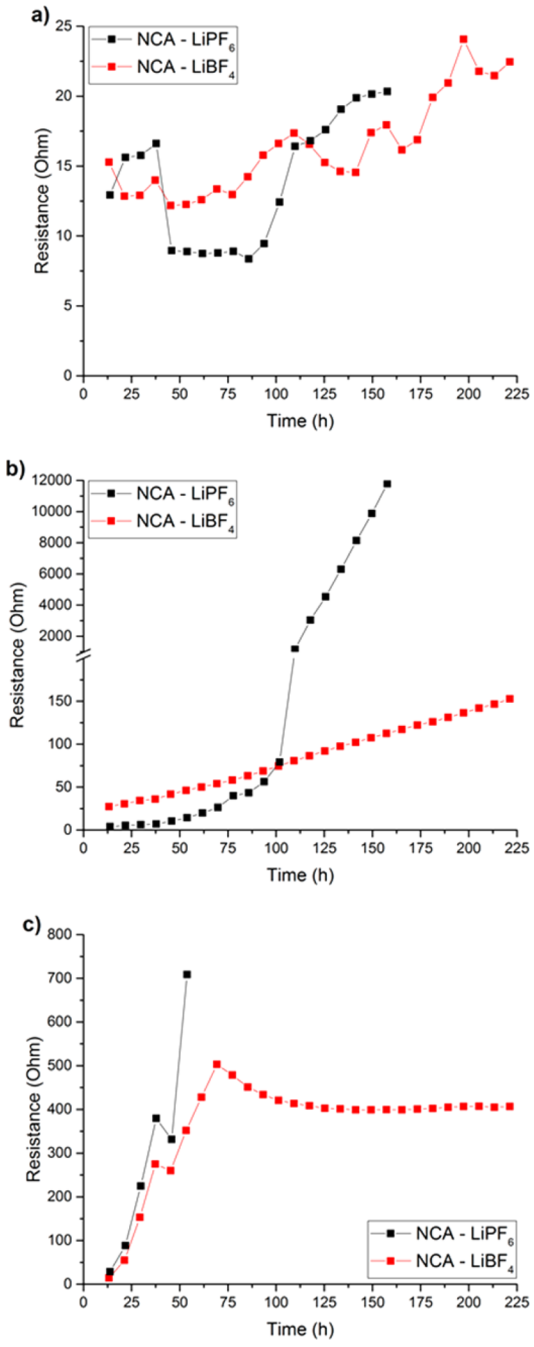

Figure 7. R1, R2, and R3 impedance values extracted from the $LiPF_6$ (black) and $LiBF_4$ (red) impedance spectra in Figure S10 are plotted versus time in (a), (b), and (c), respectively. Note the differences in the scale of the *y* axis.

peaks, which has been previously demonstrated to be associated with the beginning of the potential shift of the negative electrode. As a result of the lack of dissolution inducing parasitic reactions, the $LiBF_4$ sample has only moderate, steady R2 impedance growth. This impedance development is due to the continuous solid−electrolyte interface formation from the reduction of the electrolyte at the negative electrode.

Importantly, Figure 7c shows that, regardless of the salt used, both samples have similar R3 impedance evolution. This is attributed to the positive electrodes' impedance development as the materials approached full delithiation. Initially, R3 impedance was measured to be 28.49 Ω for $LiPF_6$ and 13.98 Ω for $LiBF_4$. After 40 h in the potentiostatic segment, the impedances grew to 708.5 and 351.8 Ω for $LiPF_6$ and $LiBF_4$, respectively. The two R3 impedances started as very similar to each other and gradually began to deviate with time in the 4.75 V hold, but both had an ∼25-fold increase in R3 impedance associated with the delithiation reaction. Around the time when the parasitic current begins for the $LiPF_6$ sample, it becomes impossible to ascertain the R3 impedance because the impedance data correlating to the positive electrode is overshadowed by the extremely large R2 and Warburg impedances. As a result of the significantly lower cell impedance, NCA cells with $LiBF_4$ are able to be discharged with near full capacity, whereas no relithiation capacity was capable for cells using $LiPF_6$. Visual analysis of opened cells after testing shows that cells using $LiBF_4$ have significantly less transition-metal deposition on the lithium negative electrode than do their $LiPF_6$ counterparts. The reduced transition-metal deposition on the anode (Table 2) is likely the origin of the 1−2 order of magnitude lower impedance observed in cells with $LiBF_4$.

Evolution of the Surface. To study the influence of Li_2CO_3, native to the $R\bar{3}m$ materials' surfaces, toward the deleterious reactions, NCA powder was exposed to ambient air for 2 weeks to accentuate the growth of Li_2CO_3.[62] TEY mode XAS O K-edge results shown in Figure 8a compare the spectra of pristine NCA (solid lines) and NCA powder that was exposed to air for 2 weeks (dashed lines). Both the pristine and air-exposed samples show a peak at 534 eV indicative of Li_2CO_3 on the NCA's surface. However, the magnitude of the peak for the air-exposed sample is much larger than for the pristine material, signifying that exposure to air developed ample additional Li_2CO_3. Quantitative TGA experiments measured 0.12 and 0.82 wt % Li_2CO_3 for the pristine and air-exposed materials, respectively. The increase in Li_2CO_3 content, as measured by TGA, is supported by the significantly larger peak in O K-edge spectra. Both the air-exposed and pristine NCA powders were charged to 4.75 V, held for 10 h at 4.75 V, and then slowly discharged to 2.7 V, all while at 60 °C. The resulting O K-edge spectra is displayed in Figure 8b, which shows that the O K-edge features related to the surface Li_2CO_3 have disappeared for both samples even after discharging. Other than the slightly higher intensity around 534 eV, little difference is observed between the exposed and nonexposed materials. Even when Li_2CO_3 was intentionally grown on the NCA's surface, negligible amounts of Li_2CO_3 are measured after charging the powder to 4.75 V and holding at constant voltage. The disappearance of Li_2CO_3 may be related to the oxidation decomposition reaction that occurs at high potentials.

TEY XAS O K-edge and Ni L_3-edge results on NCA samples before and after parasitic reactions are displayed in Figure 9. Figure 9a,b shows samples utilizing $LiPF_6$ salt, whereas samples in Figure 9c,d use $LiBF_4$. To maintain the surface oxidation state, all samples were prepared from electrodes that were disassembled in the charged state (no discharge phase). The surface-sensitive O K-edge (a) and Ni L_3-edge (b) spectra for NCA in $LiPF_6$ electrolyte show a clear transformation of the transition-metal oxidation state with the length of the potentiostatic hold. NCA charged to 4.75 V at room temperature with no potentiostatic segment (blue data) shows a line shape consistent with little Ni^{2+}. Pre-exotherm samples that were charged to 4.75 V and held for 10 h at 60 °C (red data) have spectra that suggest an average Ni oxidation state of ∼2.5, matching the significant growth in a surface Ni^{2+}

DOI: 10.1021/acs.langmuir.7b00863
Langmuir 2017, 33, 9333−9353

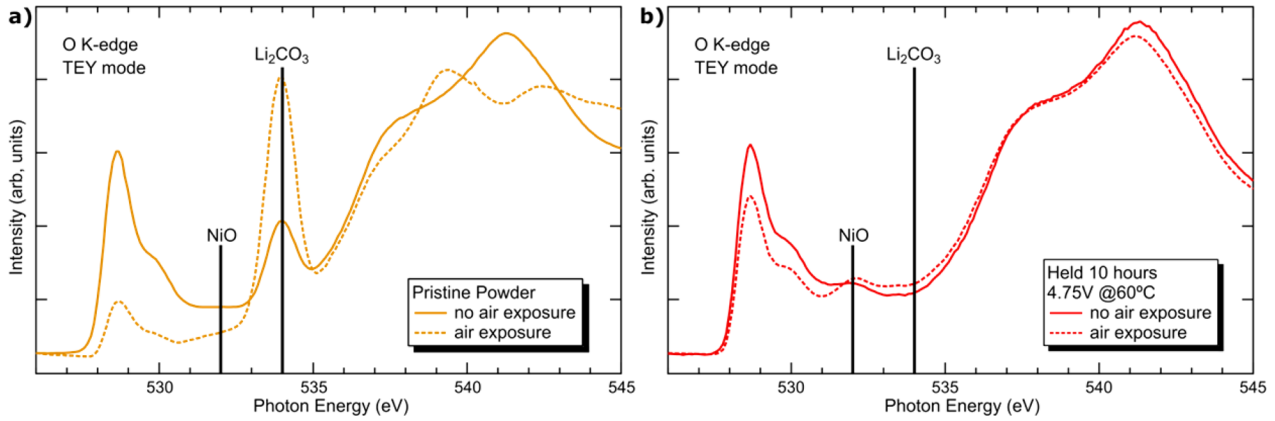

Figure 8. (a) TEY O K-edge spectra of 2-week-exposed (dashed lines) and pristine (solid lines) NCA powder. (b) TEY O K-edge spectra of powder electrodes of pristine and 2-week-exposed NCA that were charged to and held at 4.75 V and then discharged to 2.7 V while in a 60 °C incubator. All measurements were taken on beamline I09 at DLS.

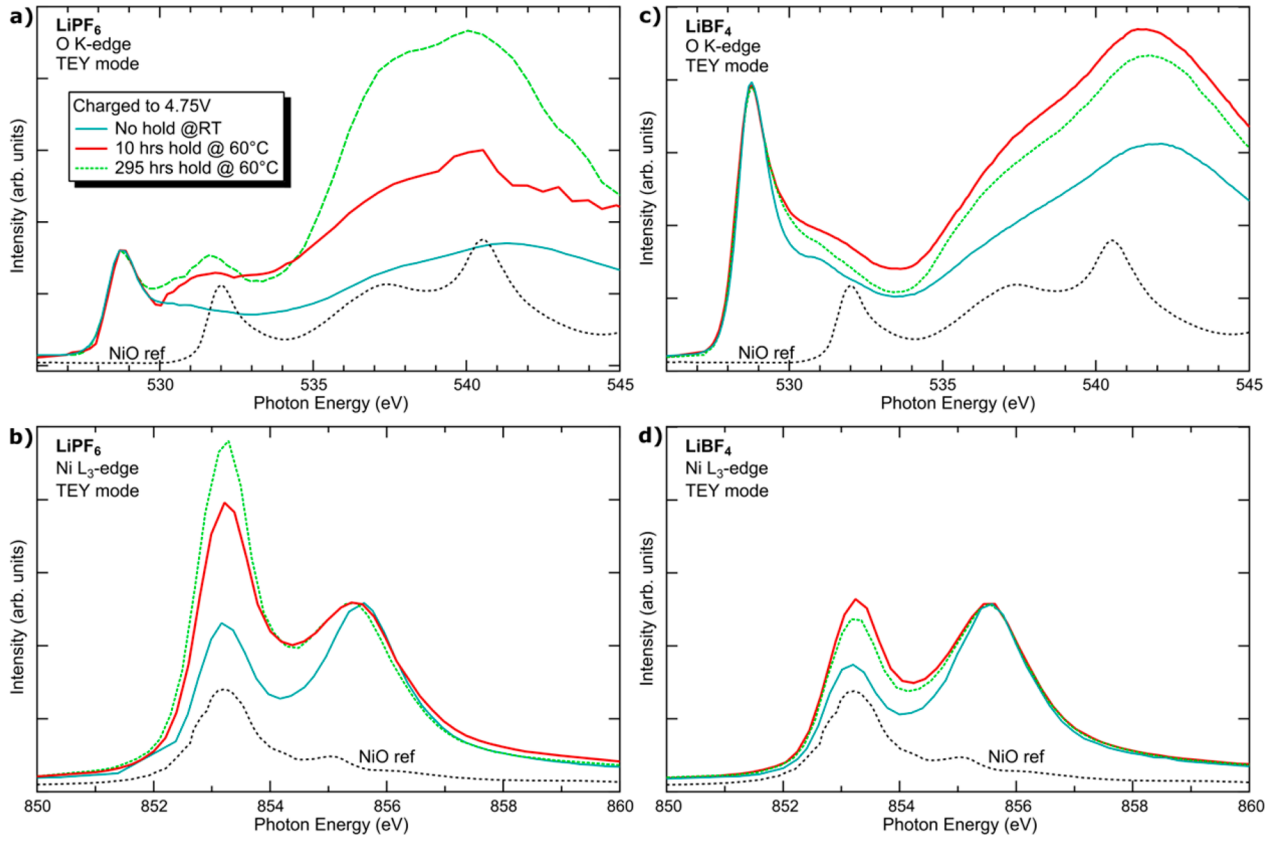

Figure 9. (a, c) TEY O K-edge and (b, d) Ni L_3-edge XAS spectra taken at ALS for NCA samples before (red) and after (green) exothermic reactions. Samples with electrolyte containing $LiPF_6$ are shown in (a, b) and those with $LiBF_4$ are presented in (c, d). All figures show reference spectra of NiO (black) and of NCA charged to 4.75 V at room temperature (blue).

containing oxide, consistent with transition-metal reduction at the surface before the exponential rise in the current and heat. This suggests that the surface decomposition precludes the potential shift in the negative electrode. These results are in agreement with the observed increase in the parasitic current prior to the potential shift of the negative electrode as detailed by the previously discussed three-electrode measurements. The line shape of the post-exotherm NCA sample (green data) reveals much more character related to the Ni^{2+} reference material, particularly the O K-edge XAS showing evidence of a feature at 532 eV consistent with the "NiO" reference. This signified that lengthening the potentiostatic hold time allows a further extension of the surface transition-metal reduction to an oxidation state of ~2, but it cannot be used as conclusive proof of the presence of a rock salt "NiO" phase. $LiBF_4$ samples show the same general trend in surface metal reduction but to a lesser degree. With no potentiostatic segment, a highly oxidized Ni environment is observed. Relative to the no hold sample, the Ni^{2+} environment associated with "NiO" increases with the 10 h hold but not to the same magnitude as for the $LiPF_6$ sample. Further potentiostatic hold up to 295 h reveals little additional growth of the "NiO". For all samples, the lack of a peak around

DOI: 10.1021/acs.langmuir.7b00863
Langmuir 2017, 33, 9333−9353

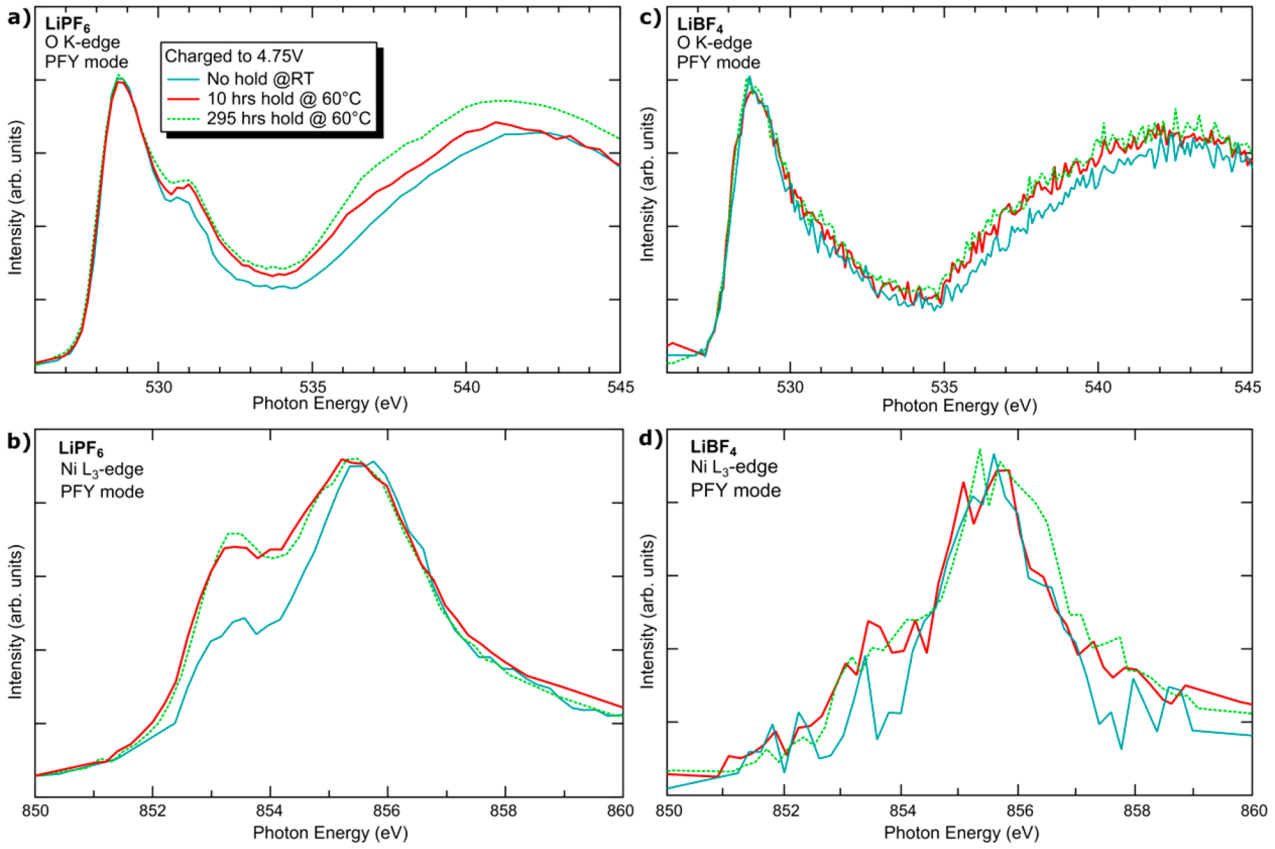

Figure 10. O K-edge (a, c) and Ni L-edge (b, d) PFY measurements taken at ALS of NCA charged to 4.75 V at room temperature (blue), pre-exotherm (red), and post-exotherm NCA (green) with either $LiPF_6$ (a, b) or $LiBF_4$ (c, d) salts.

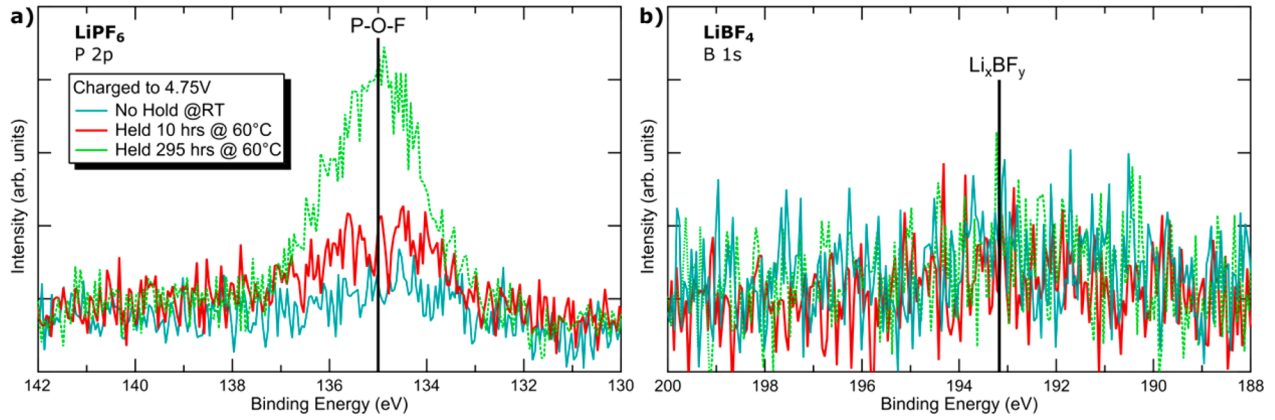

Figure 11. (a) P 2p XPS spectra for NCA electrodes with $LiPF_6$ and (b) B 1s spectra for identical samples with $LiBF_4$ salt. NCA electrodes charged to 4.75 V at room temperature are shown in blue, whereas pre-exotherm (10 h hold) and post-exotherm (295 h hold) samples are displayed in red and green, respectively.

534 eV in the O K-edge spectra suggests that negligible Li_2CO_3 was present on the surface. This observation is critical because it eliminates Li_2CO_3 as the *direct* source of the parasitic reactions.

To contrast with the surface-sensitive TEY O K-edge and Ni L-edge data for all samples introduced in Figure 9, the bulk-sensitive PFY spectra are displayed in Figure 10. As opposed to the surface-sensitive measurements, no significant changes were observed in the O K-edge PFY spectra regardless of time at the 4.75 V hold or composition of the electrolyte salt. However, there is a small reduction in the average oxidation state of Ni for $LiPF_6$ samples with increasing time at 4.75 V but no change in the $LiBF_4$ samples. Because PFY-mode XAS preferentially measures the bulk of the material, it is concluded that the majority of the changes in the transition-metal oxidation state and all of the growth of new phases is limited to the surface of the samples. This finding confirms the XRD results discussed above, which demonstrated that the structural changes on the particles' surface do not propagate into the material's bulk.

To determine if there was a presence of $LiPF_6$ salt or its decomposition products on the samples' surface, the P 2p region was also probed and is shown in Figure 11a. The P 2p results provide clear evidence of the formation of a peak centered at around 135 eV, which increases in intensity with a

DOI: 10.1021/acs.langmuir.7b00863
Langmuir 2017, 33, 9333−9353

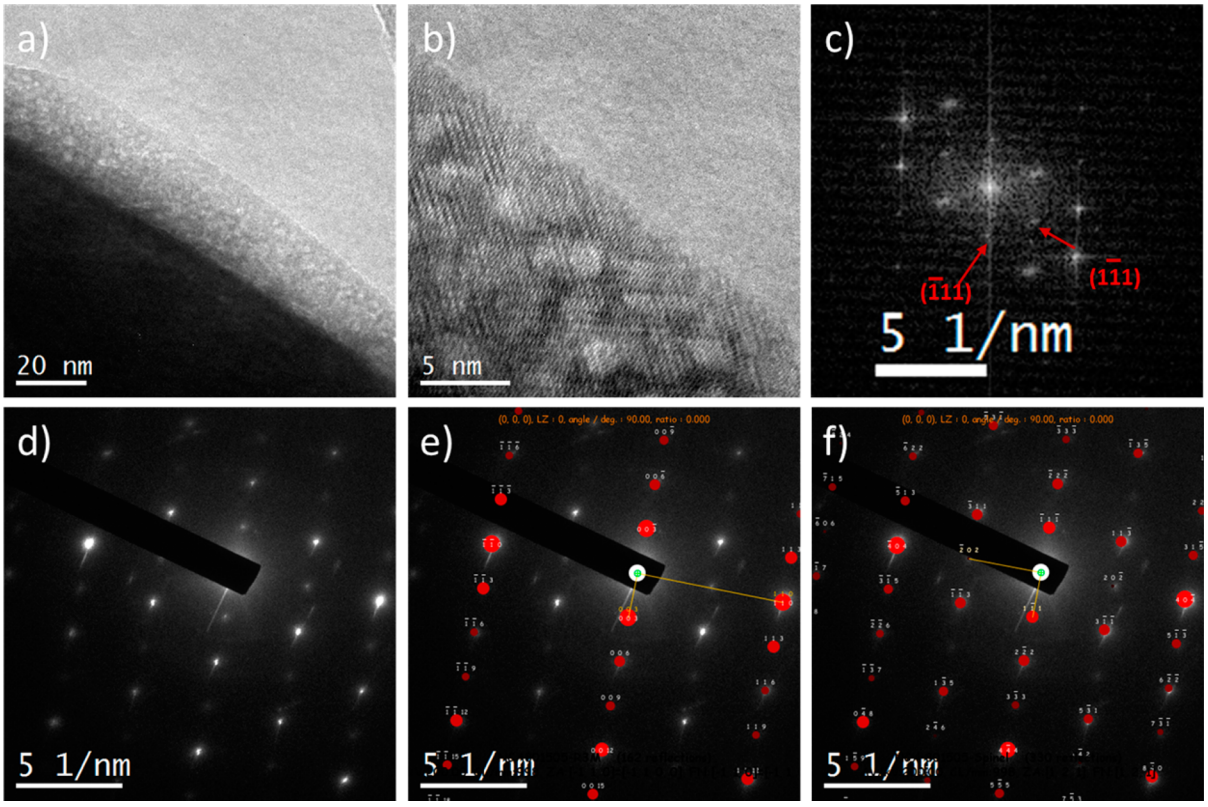

Figure 12. (a, b) HRTEM images of the surface and subsurface regions of NCA aged in $LiPF_6$ at 4.75 V, 60 °C for 10 h. The surface region in (a) is enhanced and shown in (b). (c) FFT and (d) SAED of the surface layer are also provided. The SAED image (d) is indexed with a zone axis of either $[-110]_{layered}$ or $[121]_{spinel}$ in images (e) and (f), respectively.

longer potentiostatic hold. The post-exotherm sample (green data) shows a much stronger peak than the pre-exotherm sample (red data), signifying that the exothermic reactions were the main cause of this surface species. On the basis of the P 2p and F 1s (not shown) XPS spectra, this new species was determined to be a P−O−F type material. A likely peak position for the P−O−F material is denoted in Figure 11a. The P−O−F signal is also supported by the broad intensity development in the O K-edge spectra in the region of 535−540 eV in Figure 9a. Unlike $LiPF_6$, the B 1s (Figure 11b) spectra did not present an analogous B−O−F species or even signs of deposition of the $LiBF_4$ salt. In fact, the B 1s spectra showed no significant difference between samples, regardless of the length of the potentiostatic hold, and the O K-edge XAS for $LiBF_4$ (Figure 9c) presented no evidence of any B−O−F material. The expected location for a material similar to the $LiBF_4$ salt is shown in Figure 11b.

Multiple particles of NCA aged for 10 h in $LiPF_6$ or $LiBF_4$ at 60 °C and 4.75 V were analyzed by HRTEM. As demonstrated by the HRTEM and FFT images in Figure S11, the native NCA material exhibited an $R\bar{3}m$ phase in the subsurface and surface regions. The pristine material was sometimes observed to be capped by an extremely thin (1 nm) rock-salt-like phase at the surface. In contrast, all $LiPF_6$ aged surface and subsurface regions showed a transformation to a spinel-like structure. Figure 12a shows a HRTEM image of the surface and subsurface areas of a $LiPF_6$ aged sample, and Figure 12b provides an enlarged image of the particle's surface. The phase identification is supported by FFT and SAED analyses of approximately 5 nm from the surface (Figure 12c,d, respectively). The SAED data shows a much better match to the simulated SAED pattern intensities of the $Fd3m$ spinel (Figure 12f) than to the $R\bar{3}m$ layered phase (Figure 12e). The structural transformation to a spinel-like phase within at least the first 5 nm of the NCA surface was complete and consistent from surface to surface and particle to particle. It was often observed that the structural degradation continued well into the subsurface region. The structural transformation supports transition-metal migration to the 16d octahedral sites of the spinel structure concomitant with the oxygen loss and Ni reduction as evidenced by XPS and XAS. It should be noted that one cannot conclusively state that it is of the $Fd3m$ structure because partial occupation of the former Li 3a layer by transition-metal ions are noted but the developed intensities seem to suggest ordering analogous to a spinel-like structure versus a disordered rock salt within that layer. Despite XAS results showing the evolution of Ni^{2+}, no significant reflections associated with $Fd3m$ 8a tetrahedral sites could be identified.

For HRTEM images of $LiBF_4$ aged samples (Figure 13a,b), the surface transformation to spinel-like occurred throughout at least the first 5 nm, but it was not consistent or deeply penetrated, as was observed with the $LiPF_6$ aged materials. Figure 13b demonstrates that surfaces, even within the same particle, contained a mixture of spinel, residual $R\bar{3}m$, and a very small amount of a true rock salt phase. The rock salt phase may be from the native 1 nm film of rock salt initially present on the NCA. The corresponding SAED patterns for the three surfaces in Figure 13b are presented in Figure 13c−e. All three surfaces had mainly layered structures with varying spinel reflection intensities. The spinel reflections were weak on surface 1, very weak on surface 2, and nonexistent on surface 3. In short, a transformation similar to the $LiPF_6$ case seems to be initiating

DOI: 10.1021/acs.langmuir.7b00863
Langmuir 2017, 33, 9333−9353

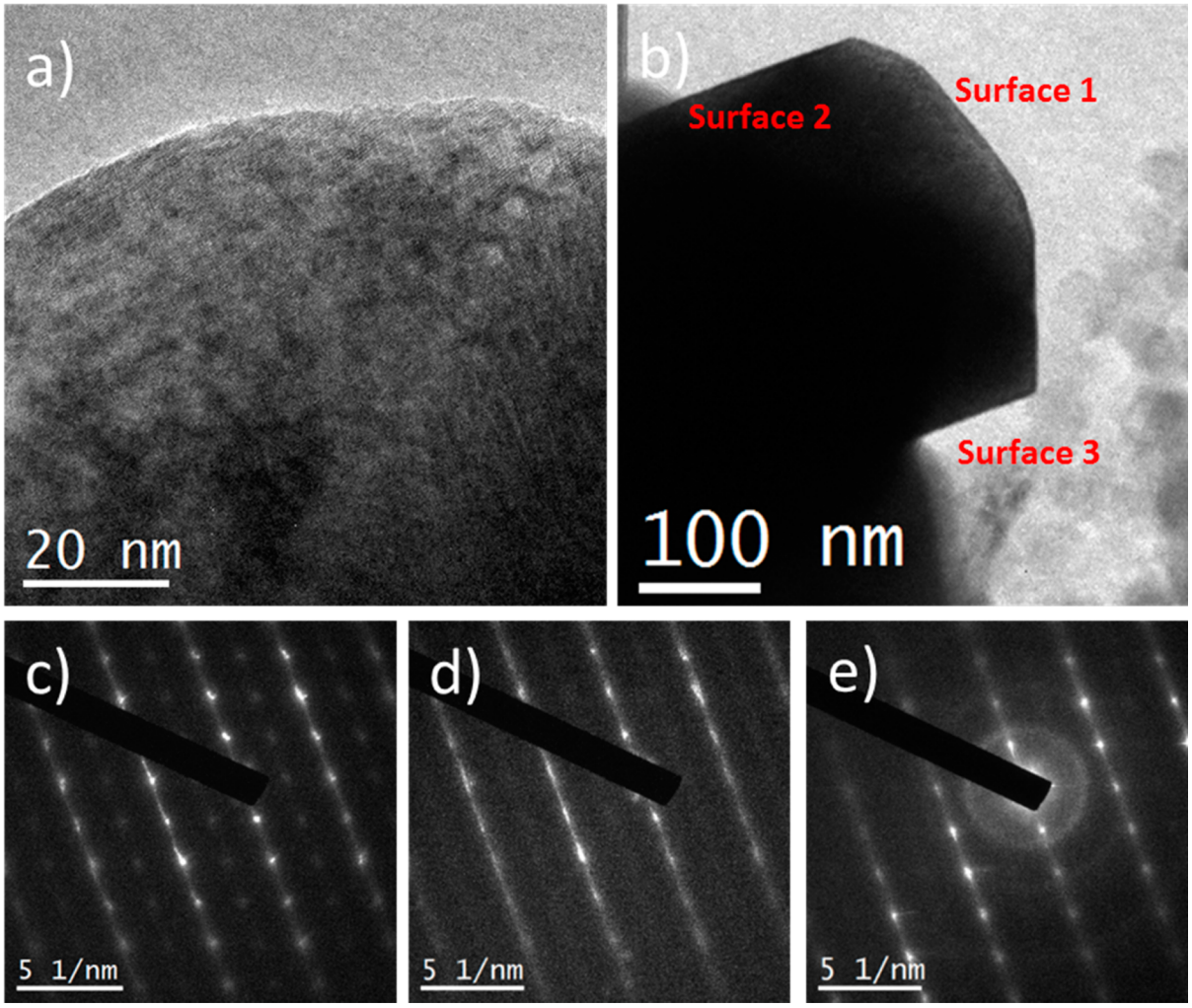

Figure 13. (a, b) HRTEM images of NCA particles aged in $LiBF_4$ at 4.75 V, 60 °C for 10 h. SAED figures corresponding to surfaces (c) 1, (d) 2, and (e) 3 in image (b) are provided. Additional rows of weak reflections in (c) are indicative of the formation of the spinel phase.

but the degree of the transformation is far less in intensity and consistency.

Interestingly, the sharp difference in contrast between the bright 20 nm surface layer and the bulk (Figure 12a) in the $LiPF_6$ sample is attributed to the significant amount of porosity observed in the surface layer. This porosity is a result of the observed transition-metal dissolution and reduces the absorption of the transmitted beam significantly. In contrast, the surface of $LiBF_4$ exposed particles (Figure 13a,b) did not show this line of contrast demarcation consistent with the reduced dissolution products. Although powder XRD experiments show that there are no structural changes to NCA throughout the bulk material (Figure 3), HRTEM results provide evidence of large structural and morphological transformations in the surface and subsurface regions. It was also observed that the $LiPF_6$ aged particles had significant surface roughening relative to the pristine material. Some surface texturing was also apparent in $LiBF_4$ samples but to a much lesser degree than what was observed for $LiPF_6$, consistent with the reduced dissolution for $LiBF_4$ aged samples.

Additional Studies. To facilitate faster analysis of new samples, coin cells were tested in a 60 °C incubator, which mimics the thermal environment required for the exothermic reactions. Incubator cells were subjected to an electrochemical testing procedure identical to that of microcalorimetry cells, but in a 60 °C isothermal environment instead of the dynamic profile used for microcalorimetry experiments. Figure S12 compares the current and accumulated capacity for duplicate microcalorimetry cells (black) and incubator cells (red). Both sets of cells show nearly indistinguishable exothermic reaction profiles during the 4.75 V, 60 °C hold. The earlier onset of parasitic reactions and slightly higher measured capacity for the incubator cells can be attributed to the isothermal conditions at 60 °C. Lower temperature phases (30 and 45 °C) for the microcalorimetry cells cause periods of reduced leakage currents and result in a lower measured capacity. The reproducibility of the parasitic reactions between the microcalorimetry and incubator cells enables a higher throughput approach to studying these particular cathode−electrolyte interactions by just measuring the current response as a test for the propensity of transition-metal dissolution.

If such reactions are surface-induced, then the magnitude and/or kinetics of the dissolution should be increased with higher surface-area NCA. High-surface-area (SA) NCA was developed by ball milling pristine NCA powder at 400 rpm for 15 min in an Ar atmosphere. XRD results (not included) showed no evidence of new phase development or structural degradation of the pristine material as a result of milling. To investigate the effect of native Li_2CO_3 on the surface of NCA, which can develop with ambient exposure during processing,

DOI: 10.1021/acs.langmuir.7b00863
Langmuir 2017, 33, 9333−9353

portions of both the pristine and high-surface-area samples were exposed to the ambient atmosphere to develop Li_2CO_3 on the particles' surface as discussed in the preceding section. It is important to note that the two samples were not exposed to ambient air at the same time, resulting in exposure to potentially different degrees of humidity, temperature, and air composition. Regardless of when the samples were exposed, 2 weeks was observed to be ample time for Li_2CO_3 growth. Other experiments show that additional exposure beyond 2 weeks resulted in minimal increases in Li_2CO_3 content, signifying that the reaction rate has been reduced to incremental levels.

For all samples, the surface area was measured using BET analysis, whereas an estimate of the Li_2CO_3 related content was determined by TGA.[63] Results of the BET and TGA experiments are shown in Table 1. Milled NCA was found to have a surface area of 7.40 m^2/g, around 16 times larger than the pristine sample (0.46 m^2/g). The high-surface-area NCA had only minimal Li_2CO_3 development relative to the original material: 0.24 versus 0.12 wt %, respectively. Two-week-exposed NCA and 2-week-exposed, high-surface-area NCA samples had Li_2CO_3 contents of around 0.82 and 1.74 wt %, each a roughly 7-fold increase compared to the nonexposed precursors. The surface areas of the exposed samples were assumed to be little changed as a result of exposure, based on BET measurements of similar NCA samples that were exposed to the ambient atmosphere.

Table 1. Surface Area, Li_2CO_3 Content, and Average Discharge Capacities for Four Variations of NCA[a]

sample	surface area (m^2/g)	Li_2CO_3 content (wt %)	discharge capacity in $LiPF_6$ (mA h/g)	discharge capacity in $LiBF_4$ (mA h/g)
pristine NCA	0.46	0.12	0	165.5
high SA NCA	7.40	0.24	0	140.1
2-week-exposed NCA		0.82	0	173.5
2-week-exposed high-SA NCA		1.74	0	137.7

[a]Measured surface area and Li_2CO_3 content for the four NCA variations are provided. After the constant-voltage phase, cells were discharged at 5 mA/g to 2.7 V. The average discharge capacities after testing with either 1 M $LiPF_6$ or 1 M $LiBF_4$ in EC/DMC (1:1) are included.

Parasitic reactions for incubator cells made of pristine NCA, the 7.40 m^2/g NCA, and their exposed analogs are shown in Figure 14a,b for cells with $LiPF_6$ and $LiBF_4$ salt, respectively. To accommodate the higher-surface-area NCA samples, a modified electrode composition with additional binder and carbon black was used, as described in the Experimental Section. All active electrodes in Figure 14a,b use this new composition to enable direct comparisons between samples. The parasitic peak shape is similar for all cells in Figure 14a, and despite the change in electrode composition, it is comparable to the structure of exothermic reactions previously presented.

Comparison of the higher surface area, 7.40 m^2/g NCA (red) to 0.46 m^2/g NCA (black) in Figure 14a, clearly demonstrates an earlier onset for parasitic reactions related to dissolution; however, there is no significant change in the measured corrosion capacity. Because the observed reactions take place on the surface of the NCA particles, it is expected that

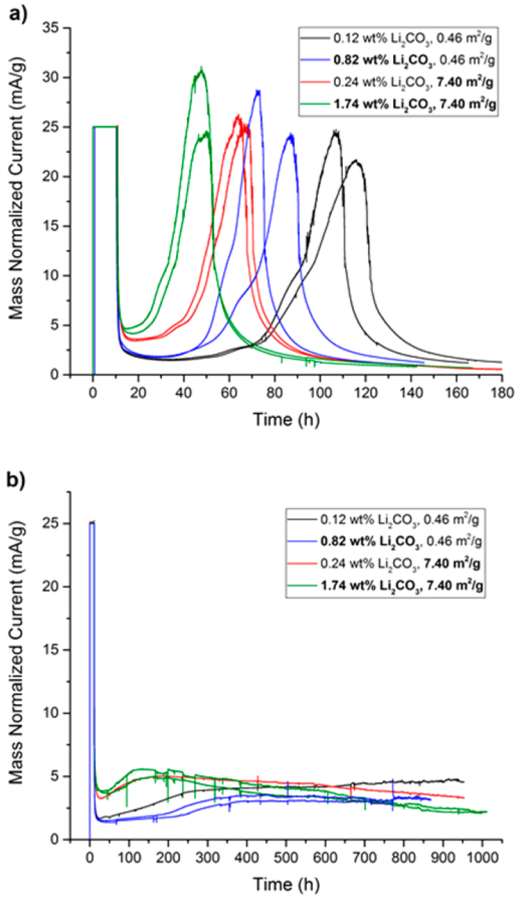

Figure 14. Comparison of the current from the parasitic reactions for 0.12 wt % Li_2CO_3, 0.46 m^2/g (black), 0.82 wt % Li_2CO_3 (blue), 0.24 wt % Li_2CO_3, 7.40 m^2/g (red), and 1.74 wt % Li_2CO_3, 7.40 m^2/g (green) NCA materials when using (a) $LiPF_6$ or (b) $LiBF_4$ salt in a EC/DMC (1:1) solvent. All samples were charged at 25 mA/g to 4.75 V and then held potentiostatically at 4.75 V in a 60 °C incubator.

increasing the number of potential sites for reaction would result in increased dissolution, which manifests itself as an accelerated reaction. The 0.82 wt % Li_2CO_3 NCA sample (blue) also had a quicker initiation of the exotherm relative to the initial 0.12 wt % Li_2CO_3 NCA, although not as rapid as the 0.24 wt % Li_2CO_3, 7.40 m^2/g material. As with the increase in surface area, increasing Li_2CO_3 content did not result in additional total capacity. The critical indicator is the time it takes for the peak current to develop because it is a direct indication of both the quantity and kinetics of the dissolution products. The total corrosion capacity is relatively meaningless as all cells will shut down once the impedance of the negative increases to a critical value. Of all samples, the 1.74 wt % Li_2CO_3, 7.40 m^2/g material (green), representing the highest Li_2CO_3 content and surface area, has the shortest time to the peak in exothermic reactions. The combination of high surface area and increased Li_2CO_3 content causes the parasitic current to develop within a couple of hours of reaching 4.75 V, around 10 h quicker than the next sample: 7.40 m^2/g NCA. In summary, a trend toward faster initiation of the dissolution reaction is observed with both increasing surface area and additional Li_2CO_3 wt %.

The impact of surface area and Li_2CO_3 content on the parasitic reactions of NCA with the 1 M $LiBF_4$ EC/DMC (1:1) electrolyte is presented in Figure 14b. As shown in Figure 6, the

DOI: 10.1021/acs.langmuir.7b00863
Langmuir 2017, 33, 9333−9353

Table 2. Co and Ni Dissolution Measurements from NCA Determined by ICP−AES

	1 M $LiPF_6$EC/DMC (1:1)				1 M $LiBF_4$EC/DMC (1:1)			
sample description	total Co dissolution (ug)	total Ni dissolution (ug)	%Co dissoluted	%Ni dissoluted	total Co dissolution (ug)	total Ni dissolution (ug)	%Co dissoluted	%Ni dissoluted
baseline cell	1.116[a]	3.497	0.095[a]	0.056	7.444[a]	7.444[a]	0.495[a]	0.093[a]
4.5 V−10 h	1.265[a]	2.530	0.091[a]	0.034	7.301[a]	7.301[a]	0.558[a]	0.105[a]
4.5 V−10 h	1.265[a]	3.274	0.082[a]	0.040	7.370	32.012	0.534	0.436
4.5 V−25 h	1.339[a]	8.928	0.080[a]	0.100	7.560[a]	7.560[a]	0.409[a]	0.077[a]
4.5 V−25 h	1.116[a]	11.904	0.064[a]	0.128	7.430[a]	14.860	0.450[a]	0.169
4.75 V−10 h	8.928	57.288	0.591	0.713	7.356[a]	27.492	0.455[a]	0.320
4.75 V−10 h	13.392	89.280	0.769	0.966	7.220[a]	36.100	0.384[a]	0.362
4.75 V−25 h	37.944	223.200	2.115	2.342	9.613	56.940	0.560	0.625
4.75 V−25 h	40.920	238.080	2.226	2.438	10.263	68.176	0.561	0.701
4.75 V−175 h	194.483	1054.694	10.349	10.566	53.820	299.000	3.167	3.312
4.75 V−175 h	187.748	1006.327	10.994	11.095	47.852	276.645	2.914	3.171

[a]Denotes that the minimum detection limit was reached and that the listed value is the maximum possible.

degradation reactions for NCA with $LiBF_4$ salt have a fundamentally different profile than with $LiPF_6$ salt. The current profiles shown in Figure 14b are similar to those for the $LiBF_4$ microcalorimetry cells; a small increase in current plateaus into a prolonged phase of elevated current. However, unlike the microcalorimetry cells, the $LiBF_4$ incubator cells were held under potentiostatic conditions for nearly 1000 h before being discharged. All samples maintained significant current throughout the entire test, indicating that no passivation of the decomposition reaction occurred. The 0.24 wt % Li_2CO_3, 7.40 m^2/g (red) and 1.74 wt % Li_2CO_3, 7.40 m^2/g (green) NCA samples rapidly show an increase in current after being charged to 4.75 V, correlated to the quick development of degradation reactions. However, the rise in current for 0.12 wt % Li_2CO_3, 0.46 m^2/g (black) and 0.82 wt % Li_2CO_3, 0.46 m^2/g NCA (blue) was much more gradual. As with the $LiPF_6$ sample set, the faster kinetics for the higher surface-area materials can be attributed to the larger electrode−electrolyte interfacial area.

After the constant voltage segment, cells were discharged to 2.7 V at 5 mA/g at 60 °C. Average discharge capacities for all cells in Figure 14a,b are presented in Table 1. When tested with $LiPF_6$ salt, all cell variations demonstrated no discharge capacity. However, all of these cells had an OCV below 3 V prior to discharge, and half had an OCV below the 2.7 V threshold. As previously shown, the low OCV is a result of the excessive transition-metal deposition on the negative electrode. Separate experiments show that when the negative electrode is replaced with a new piece of Li foil and fresh electrolyte the post-exotherm NCA can be relithiated with a capacity of up to 150 mA h/g. As described earlier, for post-exotherm cells using $LiPF_6$ drastic impedance buildup on the negative electrode is observed, which makes removing Li ions during discharge exceedingly difficult. $LiBF_4$ cells fared much better, showing OCV values greater than 4.54 V and average discharge capacities of between 140 and 175 mAh/g after 850−1000 h at 60 °C and 4.75 V. Visual observations show that negative electrodes from $LiBF_4$ samples have significantly less transition-metal plating, even after much longer times at 4.75 V and 60 °C. Impedance scans of other $LiBF_4$ samples measure only moderate levels of impedance on the negative electrode, supporting our visual observations.

Quantitative dissolution data was obtained from an additional set of 60 °C cells that were specially prepared and tested using ICP−AES analysis. The ICP−AES samples were pristine NCA materials and used one of two different maximum potentials (4.5 or 4.75 V), a 10, 25, or 175 h CV period and either $LiPF_6$ or $LiBF_4$ salt in EC/DMC (1:1). The left column of Table 2 contains the sample description that provides information on the maximum charging potential and duration of the constant voltage segment. All samples were tested with both $LiPF_6$ and $LiBF_4$ salts to enable direct comparisons of the voltage and time in the potentiostatic hold as a function of salt. Samples with total dissolution data denoted by footnote a indicated that the minimum detection limit for ICP−AES was reached, and the maximum possible value is listed.

Baseline cells, composed of all cell parts and active materials but having no electrochemical or thermal testing, were made using each electrolyte salt. These samples established baseline Co and Ni dissolution levels from native acids that may be present in the electrolyte which may have reacted with the stainless steel components of the coin cell hardware. Because the ICP−AES measurements measure only the Co and Ni deposited on the negative electrode and trapped within one of the two separators, the technique will always provide results slightly below the true degree of dissolution. Comparison of the NCA-$LiPF_6$ samples charged to 4.5 V shows that regardless of whether a 10 or 25 h constant voltage segment (CV) was used, no significant Co dissolution was measured. Although absolute amounts of Ni were measured in all of these samples, the degree of dissolution was still minimal, with ∼0.04 and ∼0.12% for the 10 and 25 h potentiostatic holds, respectively. In contrast, NCA-$LiPF_6$ samples charged to 4.75 V have markedly higher levels of both Co and Ni dissolution. %Co and %Ni dissolution results for the 10 h CV samples were ∼0.68 and ∼0.84, whereas the analogous 25 h CV samples had extremely high values of ∼2.17 and ∼2.39%. Clearly, the magnitude of dissolution increases rapidly with higher potentials and with extended time in the potentiostatic hold. In fact, below 4.75 V the measured dissolution products were either indistinguishable or insignificant compared to the baseline sample.

NCA-$LiBF_4$ samples, although showing much less dissolution, provide supporting evidence of increased transition-metal dissolution with higher potentials and a longer potentiostatic hold. Compared to the $LiBF_4$ baseline sample, both the 10 and 25 h, 4.5 V $LiBF_4$ samples had negligible levels of Co dissolution. Only one of the duplicate cells for each the 4.5 V 10 h and 4.5 V, 25 h samples had a significant degree of Ni dissolution: 0.436 and 0.169%, respectively. For the $LiBF_4$ samples at 4.75 V, ∼0.34% for 10 h CV and ∼0.66% for 25 h

DOI: 10.1021/acs.langmuir.7b00863
Langmuir 2017, 33, 9333−9353

CV were measured reproducibly for both cells. Although enhanced relative to 4.5 V, these values are approximately 300% less than for analogous $LiPF_6$ samples. For both $LiPF_6$ and $LiBF_4$ salts, NCA samples were held at 4.75 V until parasitic reactions were completed (175 h potentiostatic phase) to quantitatively determine the amount of Co and Ni dissolution in an extreme scenario. In $LiPF_6$, the 4.75 V, 175 h samples had ~10.67% Co and ~10.83% Ni dissolution, whereas in $LiBF_4$, ~3.04% Co and ~3.24% Ni dissolution was observed. Samples using $LiPF_6$ again exhibit approximately 3 times the Co and Ni dissolution rates compared to the $LiBF_4$ samples, which supports the conclusions determined previously by electrochemistry, XAS, and HRTEM. Importantly, the analysis of the %Co and %Ni dissolution results from the ICP−AES data shows that the dissolution rates for Co and Ni are nearly identical for every sample, suggesting that there is no preferential etching of Co or Ni from the positive electrode.

Discussion. A number of studies have explored the surface and subsurface evolution of $R\bar{3}m$ compounds including NCA, but most of these have been performed at voltages <4.4 V and very few at full delithiation. On one hand, this study could be taken as an extrapolation of the failure modes observed at lower potentials and elevated temperature. On the other hand, voltages above 4.4 or 4.5 V can activate new decomposition processes, particularly those related to carbonates because many commence anodic decomposition at such potentials. The goal of this particular research was to explore the role of the electrolyte in inducing failure modes, especially dissolution, at the surface of the fully delithiated $R\bar{3}m$ materials without the mechanochemically related failure modes induced by cycling. Clearly there is an intimate relationship between the electrolyte and the stability of the positive electrode at high potentials.

On the basis of the surface characterization of NCA by XPS, TEY-mode XAS, FFT via HRTEM, and SAED, one could conclude that exposure to $LiPF_6$ and $LiBF_4$ electrolytes induces a structural transformation to a phase composed of a Ni^{2+} environment consistent with a spinel-like structure and that the transformation is much more pronounced in the $LiPF_6$ electrolyte. The reaction seems to passivate or proceed very slowly in $LiBF_4$ versus a more intense evolution when using $LiPF_6$. One should not infer from this statement that the diffusion of O out of the structure or the back diffusion of Ni^{2+} is enhanced when $LiPF_6$ is present, leading to a thicker transformation at the surface. An inspection of the HRTEM images suggests that the etching induced by dissolution when $LiPF_6$ is used allows a porous surface to develop. This porous surface enables electrolyte penetration into the pores and results in a deeper transformation of the surface to the spinel-like phase. Therefore, the thicker surface phase is not necessarily a result of enhanced oxygen and Ni^{2+} diffusion but rather enhanced access to the subsurface structures via etched porosity. As such, if dissolution-induced porosity could be limited, then the depth of the spinel-like surface transformation could be limited also.

The surface transformation that induces the impedance increase is classified as spinel-like within this article because of the fact that there is a degree of transition-metal occupation developing in the octahedral 3a Li sites in $R\bar{3}m$ that is not due to significant tetrahedral site (8a in $Fd3m$) occupation. This leads to a very important question of what a partially occupied 3a site (16d in $Fd3m$) is called crystallographically, especially in the context of the spectrum of the spinel to rock salt transformation where the rock salt would signify full transition-metal occupation of the 3a site (vs 25% for spinel). In this article, we refer to it as spinel-like because the electron diffraction suggests that a degree of transition-metal ordering within the octahedral sites has developed. It is likely that the 3a occupation may have exceeded the 25% required for spinel on the path toward rock salt. Such defects would also enable proper charge balancing such that bivalent Ni could be observed in a spinel-like structure. This is the subject of a following paper and is too detailed to be discussed herein. A takeaway relative to the electrochemistry is that the surface transformation can be protective and passivating by limiting further back diffusion of Ni or forward diffusion of oxygen, but if a porous structure develops, the extension of the transformation layer can be extended significantly. This extension does not necessarily increase the impedance significantly because the electrolyte penetrates this porous layer and allows effective transport of Li^+ deeper through the surface-transformed regions. Indeed, both $LiPF_6$ and $LiBF_4$ electrolytes increase the positive electrode impedance about 10-fold as a result of the surface transformation after about 10 h at 4.75 V and 60 °C even though the thickness of the transformed layer is drastically different.

The quantitative dissolution data via ICP was revealing in its reproducibility and its systematic correlation to the onset of the peak in current and exotherm observed in the potentiostatic electrochemical data. The latter suggests that such studies can be used in lieu of the ICP analysis to extract qualitative comparisons as long as the structure of the electrochemical cell and subsequent tortuosity of the electrolyte through the cell are kept consistent. The quantitative analysis tied to the electrochemical data revealed these conclusions regarding dissolution in $LiPF_6$ EC/DMC electrolytes:

i. Dissolution correlates with an increase in surface area.
ii. Dissolution correlates with an increase in surface Li_2CO_3.
iii. Dissolution correlates with the cell voltage.
iv. Dissolution correlates with potentiostatic time.

The dissolution products are intimately tied to the presence of $LiPF_6$ because 300% less dissolution is observed for samples containing $LiBF_4$. This dissolution is not a result of hydrolysis from the HF native to $LiPF_6$ solutions because the dissolution products trend very significantly with the state of charge, time at elevated voltage, and subsequent reduction of the NCA surface. The voltage dependency of the dissolution product is consistent with results shown earlier for $LiCoO_2$ and other materials.[3,64] These results, combined with the fact that the magnitude and intensity of the dissolution are correlated with the material (NCA vs LCO), the surface area, and the surface chemistry (especially Li_2CO_3 content), clearly cement the symbiotic relationship among the surface, surface chemistry, and decomposition of the $LiPF_6$-based electrolyte. A few mechanisms have been published on the interaction of $LiPF_6$ leading to the catalytic decomposition of $LiPF_6$ at high potentials, which creates an oxidized PF_6 radical and HF. This is despite the fact that $LiPF_6$ is in theory a stable electrolyte salt at high voltage.

The impact of dissolution on the mixed potential of the negative electrode was very significant. The potential shift occurring at the positive and negative electrodes is undetectable under constant voltage charge, but three electrode studies revealed that the Li negative electrode gradually developed a mixed potential approximately equivalent to that of the redox potential of Ni/Ni^{2+}, resulting in a greater than 2 V shift. Even a

DOI: 10.1021/acs.langmuir.7b00863
Langmuir 2017, 33, 9333−9353

<0.05 V shift in the positive electrode potential induced by the increase in the negative electrode potential would be detrimental to the long-term performance of an electrochemical cell. The effective potential of the positive electrode will increase, thus launching the positive electrode into an accelerated continuous cycle of dissolution and potential increase, all while the two-electrode voltage is invariant. Even small potential shifts in a nonfully delithiatiated positive electrode could induce such a cycle to occur over a long period of time. The main importance of transition-metal dissolution to Li ion batteries is the metal deposition on the negative electrode, which even in small amounts induces very catalytic reactions and modification of the SEI formed on graphite and alloy negative electrodes. Although most studies have not shown that the deposition product is a metallic species, our data herein shows the presence of metallic Ni and the probable identification of metallic Co, present on the Li metal negative electrode. In a research scenario, tracking the propensity of a material to induce dissolution within an electrolyte, beyond simple HF acid attack from the native HF in equilibrium with $LiPF_6$, has been problematic. Using this accelerated cycle of dissolution, the potential shifts while held at constant two-electrode potential show a surprisingly reproducible methodology for studying the degree to which positive electrode surfaces and electrolytes induce dissolution. No doubt, refined three-electrode cells tracking small potential changes will make the resolution of the technique even more effective.

Both the baseline exothermic heat generation and corrosion current were observed to increase systematically with voltage and temperature. The background current at 4.75 V and 60 °C is likely due to the anodic decomposition of the carbonate solvent because the current and heat generated were virtually identical for the $LiBF_4$ and $LiPF_6$ EC/DMC electrolytes before the dissolution-induced voltage shift in $LiPF_6$ electrolytes. A few model reactions based on electrolyte characterization have been proposed by others. When factoring in the catalytic NCA, the most obvious case of NCA surface and salt independent solvent interactions rests in a simplified reaction of 1 and 2, which are intimately tied.

$$2NiO_2 \rightarrow 2NiO + O_2 \quad (1)$$

$$CH_3OCO_2CH_3(DMC) + 3O_2 \rightarrow 3CO_2 + 3H_2O \quad (2)$$

This is based on the overoxidation reactions proposed by Kumai et al. for CoO_2 ($Li_{1-x}CoO_2$) leading to Co_3O_4. The generation of water was confirmed by their analysis.[65] Both our XPS and HRTEM results support the reduction of Ni^{3+} to Ni^{2+} and the formation of a surface layer composed of a Ni^{2+}-rich oxide "spinel", which provides evidence that these reactions are likely accelerated by the oxidation of the solvent. However, in the $LiBF_4$ case the Ni^{2+} and "NiO" surface content is much lower, suggesting effective passivation. This leads us to the second question of why "NiO" would be effective in passivating the $LiBF_4$ electrolyte but not as much with $LiPF_6$. As discussed above, much relates to the propensity of $LiPF_6$ to aggressively etch the surface. This promotes curiosity as to what the exact decomposition reactions of the salt are and their influence on the NCA surface as we have discussed above with respect to dissolution.

$LiBF_4$ is quite oxidation-resistant:

$$LiBF_4 \rightarrow LiF + BF_3 \quad (3)$$

In contrast, $LiPF_6$ itself decomposes easily:[66]

$$LiPF_6 \rightarrow LiF + PF_5 \quad (4)$$

In traces of water, a further decomposition also develops:

$$PF_5 + H_2O \rightarrow 2HF + POF_3 \quad (5)$$

or

$$LiPF_6 + H_2O \rightarrow LiF + 2HF + POF_3 \quad (6)$$

In both reactions, the presence of even minute amounts of H_2O, either native or byproduct, rapidly shifts the mechanisms toward the production of POF_x products and HF.[67] Clearly, the presence of $LiPF_6$ resulted in the decomposition products of Li−P−O−F present on the basis of our XPS results. The HF will then proceed to attack the NCA surface regardless of if it has already transformed to "NiO". The fact that all characterization shows the presence of the "NiO" spinel suggests that the solvent decomposition reaction precedes any HF attack. Assuming a simplified surface of "NiO", the reaction would then be expected to proceed by way of

$$NiO + 2H^+ \rightarrow Ni^{2+} + H_2O \quad (7)$$

The water produced will further react with $LiPF_6$ and also cause H_2 production at the negative electrode by the reduction of either H_2O or HF. NiF_2 could also be produced by interaction with the HF, but there is very little evidence of NiF_2 on the surface of the NCA reacting at 4.75 V. The reason likely rests in the fact that NiF_2 is relatively soluble in carbonates, especially if nickel oxyfluoride species are produced. An important question remains as to what complexes allow the diffusion of the transition metals through the electrolyte and deposit on the negative electrode. This could be by way of simple solvated divalent cations charged balanced by PF_6^- anions. A comprehensive analysis of the 4.7 V $LiNi_{0.5}Mn_{1.5}O_4$ spinel, which also has transition-metal dissolution challenges,[56] revealed the formation of a variety of $Mn^{2/3+}$ and Ni^{2+} complexes with β-diketonate ligands when linear and cyclic carbonates were anodically decomposed in the presence of the spinel.[68] These partially polymerized films dissolved in the electrolyte solution and migrated to the negative electrode.

Devoid of carbonate solvent oxidation and the O_2 contribution given by the reduction of the NCA, we must also be cognizant of the following reactions that may be generated at the surface of the nonoxide positive electrode components. Density functional theory suggests the formation of molecular HF from the proton abstraction from the carbonate species at high voltages (>4.5 V) for DMC/PF_6^- and DMC/BF_4^- scenarios.[69] Indeed, this reaction may proceed to a degree as we observe a small but systematic increase in voltage-induced dissolution products even when utilizing $LiBF_4$. It has been theorized in studies based on $LiMn_2O_4$ that the PF_6^- anion is oxidized by the positive electrode leading to PF_6° which then reacts with carbonate electrolytes to form insoluble oxyfluorophosphate compounds.[70] Another model has been presented by Aoshima et al. in their work based on delithiated $LiMn_2O_4$. They propose the decarboxylation of the carbonate solvent resulting in the formation of EtOH + CO_2 + C_2H_2.[8] They then propose that EtOH reduces MnO_2 to MnO resulting in the formation of AcOEt and H_2O. NCA could follow a similar reaction pathway where the water produced will then interact with $LiPF_6$ per eqs 5 and 6.

The impact of Li_2CO_3, which we observed to accelerate dissolution, deserves particular attention. It is clear from the

DOI: 10.1021/acs.langmuir.7b00863
Langmuir 2017, 33, 9333−9353

surface characterization that Li_2CO_3 is consumed from the surface of the NCA. Excess Li_2CO_3 has long been known to be highly detrimental to the stability of $LiCoO_2$[63] and NMC.[71] Li_2CO_3 is a particular nemesis of NCA because even brief exposures of NCA to an ambient processing environment will induce a very thin coating of Li_2CO_3. In addition, Li_2CO_3 is known to oxidize from the surface of NCA (reaction 8), resulting in the formation of CO_2 and O_2.[72]

$$2Li_2CO_3 \rightarrow 4Li^+ + 2CO_2 + O_2 + 4e^- \quad (8)$$

The O_2 can then react with carbonates per reaction 2, thus leading to additional water generation. Once water is generated, the traditional $LiPF_6$ hydrolysis reactions (reactions 4−6) will become prevalent. In addition, at 4.75 V and elevated temperature, we would expect thermodynamically favored reaction 9 to be accelerated.[73] However, it should also be noted that the process leading to the formation of Li_2CO_3 on the positive electrode surface has some complexity and the intermediate states leading to identifiable Li_2CO_3 may make their own contribution to the observed impact on the electrochemical properties.

$$Li_2CO_3 + LiPF_6 \rightarrow CO_2 + 3LiF + POF_3 \quad (9)$$

Once POF_3 species are generated, these react with cyclic carbonates to form CO_2 and oligoethylene oxides containing fluorophosphate end groups capped with alkyl fluoride $[OPF_2(OCH_2CH_2)nF]$.[74]

This presents an unfortunate scenario for Li-ion batteries as $LiPF_6$ offers outstanding conductivity and Al current collector passivation. Recent reports for the stability of electrolytes at high voltages have trended away from $LiPF_6$ toward $LiBF_4$.[75,76] Our results herein support this direction as significantly less dissolution was identified for electrolytes containing $LiBF_4$ as the electrolyte salt. However, this should not be taken as a quick fix to the voltage window issue with catalytic surfaces. The downside is apparent in that little passivation of the surface occurs and we observe much corrosion current and heat generation. This is undoubtedly due to the surface of the NCA acting as a catalyst to the constant generation of CO_2 gas through the anodic oxidation of the carbonate electrolyte per eqs 1 and 2.[77] The gas generation was so great that $LiBF_4$ coin cells held at 4.75 V and 60 °C physically ruptured as a result of the high pressure. Obviously, such issues can be addressed by appropriate selection of surface coatings/chemistry[78] and also additives to decompose and passivate the surface.

Serendipitously, we have performed a de facto investigation of the stability of NCA at voltages in excess of 6 V. Surprisingly, the bulk structure of the NCA and LCO survived such excursions with little phase transformation or transition-metal migration from the 3b to 3a layer. Densifications to 3D oxides of a reduced oxidation state require considerable oxygen diffusion from the bulk to the surface or back diffusion of the transition metals into the core of the structure. Under much less extreme conditions but after storage for over 2 years, Watanabe et al. showed a reduced performance of $LiCoO_2$ versus NCA positive electrodes and that the surface decomposition toward densified oxides progressed deeper in the case of $LiCoO_2$.[60] A mechanism that disrupts the diffusion of the oxygen or back diffusion of the transition metal is established in these layered compounds.

Although much focus is on the surface and subsurface reactions and their critical role in achieving practical cycling of layered compounds at full delithiation, it is only one of a series of failure modes. However, many of the failure modes attributed to the bulk may in fact be surface-related. Such an example can be found in the transition-metal movement to the 3a site in the bulk. In most but not all layered oxides, this movement requires divalent cation diffusion through the tetrahedral sites to the 3a octahedral sites. The reduction of the transition metal occurs by oxygen loss at the surface of the material, most likely catalyzed by the electrolyte reactions. During complete delithiation, there is a strong anisotropic collapse in the c lattice parameter that induces considerable strain within the structure. In one case, this can lead to dislocation effects and the blocking of diffusion pathways as well as microcracking. Microcracking and increased surface area, as long as they do not lead to electrochemical isolation, can be a good thing if the increased surface area does not induce additional access points for surface decomposition. As such, much attention to bulk transformations and their role in failure modes needs to be explored. However, all of these are addressable challenges, and there is no reason not to be optimistic about full utilization of the theoretical capacity of $R\bar{3}m$ materials in the future. Indeed, "Ni^{4+}"-rich 4.7 V transition-metal oxides of the spinel structure cycled to 4.99 V have seen stability for over 500 cycles when cycled at 50−60 °C in $LiPF_6$ or $LiBF_4$ EC/DMC.[57,76] As such, the transition-metal oxide structure plays an important role in the initiation of the decomposition reactions, and it may be no coincidence that the spinel-like transformation of the layered surface seems to passivate the layered compound from excessive electrode decomposition. However, the detrimental role of gassing remains a factor in many of these scenarios.

■ CONCLUSIONS

The characterization of NCA after long periods of potentiostatic analysis near full delithiation reveals little bulk degradation but significant transformations of the surface and subsurface structure. Surface degradation to Ni^{2+}-rich, spinel-like regions seems to be initiated by the oxidation of the electrolyte solvent through the release of oxygen by the metastable delithiated $R\bar{3}m$ NCA. Evidence suggests that the surface reduction reaction would be largely passivated if etching induced by the decomposition of the fluoride salt did not exist, especially for $LiPF_6$, which is known to readily form HF. Such etching led to a porous surface layer that enabled electrolyte access to further propagate the reaction. Extensive dissolution studies revealed a consistent 300% increase in transition-metal dissolution induced by $LiPF_6$ relative to $LiBF_4$. Such dissolution is activated by the cell voltage and likely tied to the water-producing oxidation reaction of the carbonate solvents. The dissolution of Co and Ni occurred in stoichiometric ratios consistent with the original stoichiometry of the NCA parent material. Fine analysis by *Operando* microcalorimetry and potentiostatic studies reveals that dissolution can be extensive enough to induce a large potential shift in the negative electrode, which was confirmed by three-electrode electrochemical analysis. A detailed dissolution study using the aforementioned method and/or ICP analysis revealed increased transition-metal dissolution with the use of $LiPF_6$ versus $LiBF_4$, with increased surface area and with increased quantities of Li_2CO_3 degradation products present on the surface of NCA after atmospheric exposure.

DOI: 10.1021/acs.langmuir.7b00863
Langmuir 2017, 33, 9333−9353

■ ASSOCIATED CONTENT

Supporting Information

The Supporting Information is available free of charge on the ACS Publications website at DOI: 10.1021/acs.langmuir.7b00863.

Additional microcalorimetry figures and three-electrode cell experiments as well as corresponding EIS results, which compare the impedance development from $LiPF_6$ and $LiBF_4$ electrolytes. XRD, EDS, and HRTEM results are also included and provide supporting evidence of the structural transformations on the positive and negative electrodes. (PDF)

■ AUTHOR INFORMATION

Corresponding Author

*E-mail: nf147@scarletmail.rutgers.edu.

ORCID

Nicholas V. Faenza: 0000-0002-2620-4592
Louis. F. J. Piper: 0000-0002-3421-3210
Glenn G. Amatucci: 0000-0003-1905-6197

Notes

The authors declare no competing financial interest.

■ ACKNOWLEDGMENTS

This work was supported as part of the NorthEast Center for Chemical Energy Storage (NECCES), an Energy Frontier Research Center funded by the U.S. Department of Energy, Office of Science, Basic Energy Sciences under award no. DE-SC0012583. XAS experiments were performed at beamline 8.0.1 at the ALS and beamline I09 at Diamond Light Source. The work at ALS was supported by the Office of Basic Energy Sciences of the U.S. Department of Energy under contract no. DE-AC02-05CH11231. We thank Diamond Light Source for access to beamline I09 (SI 12764), which contributed to the results presented here. We also thank beamline scientists Wanli Yang at ALS and Tien-Lin Lee at Diamond Light Source for their assistance.

■ REFERENCES

(1) Amatucci, G. G.; Tarascon, J. M.; Klein, L. C. CoO_2, The End Member of the $LiCoO_2$ Solid Solution. *J. Electrochem. Soc.* **1996**, *143*, 1114−1123.

(2) Seguin, L.; et al. Structural study of NiO2 and CoO2 as end members of the lithiated compounds by in situ high resolution X-ray powder diffraction. *J. Power Sources* **1999**, *81*−*82*, 604−606.

(3) Amatucci, G. G.; Tarascon, J. M.; Klein, L. C. Cobalt dissolution in LiCoO2-based non-aqueous rechargeable batteries. *Solid State Ionics* **1996**, *83*, 167−173.

(4) Kim, Y. J.; Cho, J.; Kim, T.-J.; Park, B. Suppression of Cobalt Dissolution from the LiCoO[sub 2] Cathodes with Various Metal-Oxide Coatings. *J. Electrochem. Soc.* **2003**, *150*, A1723.

(5) Lee, K. T.; Jeong, S.; Cho, J. Roles of surface chemistry on safety and electrochemistry in lithium ion batteries. *Acc. Chem. Res.* **2013**, *46*, 1161−1170.

(6) Blyr, A.; et al. Self-Discharge of LiMn2O4/C Li-Ion Cells in Their Discharged State. *J. Electrochem. Soc.* **1998**, *145*, 194−209.

(7) Vetter, J.; et al. Ageing mechanisms in lithium-ion batteries. *J. Power Sources* **2005**, *147*, 269−281.

(8) Aoshima, T.; Okahara, K.; Kiyohara, C.; Shizuka, K. Mechanisms of manganese spinels dissolution and capacity fade at high temperature. *J. Power Sources* **2001**, *97*−*98*, 377−380.

(9) Arora, P.; White, R. E. Capacity Fade Mechanisms and Side Reactions in Lithium-Ion Batteries. *J. Electrochem. Soc.* **1998**, *145*, 3647−3667.

(10) Edström, K.; Gustafsson, T.; Thomas, J. O. The cathode-electrolyte interface in the Li-ion battery. *Electrochim. Acta* **2004**, *50*, 397−403.

(11) Martha, S. K.; et al. A short review on surface chemical aspects of Li batteries: A key for a good performance. *J. Power Sources* **2009**, *189*, 288−296.

(12) Aurbach, D.; et al. The Study of Surface Phenomena Related to Electrochemical Lithium Intercalation into LixMOy Host Materials (M = Ni, Mn). *J. Electrochem. Soc.* **2000**, *147*, 1322−1331.

(13) Aurbach, D.; et al. Review on electrode-electrolyte solution interactions, related to cathode materials for Li-ion batteries. *J. Power Sources* **2007**, *165*, 491−499.

(14) Täubert, C.; Fleischhammer, M.; Wohlfahrt-Mehrens, M.; Wietelmann, U.; Buhrmester, T. LiBOB as Electrolyte Salt or Additive for Lithium-Ion Batteries Based on LiNi 0.8Co0.15Al0.05O2/Graphite. *J. Electrochem. Soc.* **2010**, *157*, A721.

(15) Kim, G.-Y.; Dahn, J. R. ARC Studies of the Effects of Electrolyte Additives on the Reactivity of Delithiated Li1-x[Ni1/3Mn1/3Co1/3]O2 and Li1-x[Ni0.8Co0.15Al0.05]O2 Positive Electrode Materials with Electrolyte. *J. Electrochem. Soc.* **2014**, *161*, A1394−A1398.

(16) Wang, D. Y.; et al. A Systematic Study of Electrolyte Additives in Li[Ni1/3Mn1/3Co1/3]O2 (NMC)/Graphite Pouch Cells. *J. Electrochem. Soc.* **2014**, *161*, A1818−A1827.

(17) Wang, Y.; Jiang, J.; Dahn, J. R. The reactivity of delithiated Li(Ni1/3Co1/3Mn1/3)O2, Li(Ni0.8Co0.15Al0.05)O2 or LiCoO2 with non-aqueous electrolyte. *Electrochem. Commun.* **2007**, *9*, 2534−2540.

(18) Hu, L.; Zhang, Z.; Amine, K. Electrochemical investigation of carbonate-based electrolytes for high voltage lithium-ion cells. *J. Power Sources* **2013**, *236*, 175−180.

(19) Wang, H.; Jang, Y.; Huang, B.; Sadoway, D. R.; Chiang, Y. TEM Study of Electrochemical Cycling-Induced Damage and Disorder in LiCoO2 Cathodes for Rechargeable Lithium Batteries. *J. Electrochem. Soc.* **1999**, *146*, 473−480.

(20) Abraham, D. P.; Twesten, R. D.; Balasubramanian, M. Surface changes on LiNi0.8Co0.2O2 particles during testing of high-power lithium-ion cells. *Electrochem. Commun.* **2002**, *4*, 620−625.

(21) Abraham, D. P.; et al. Microscopy and Spectroscopy of Lithium Nickel Oxide-Based Particles Used in High Power Lithium-Ion Cells. *J. Electrochem. Soc.* **2003**, *150*, A1450−A1456.

(22) Hwang, S.; et al. Investigation of Changes in the Surface Structure of LixNi0.8Co0.15Al0.05O2 Cathode Materials Induced by the Initial Charge. *Chem. Mater.* **2014**, *26*, 1084−1092.

(23) Watanabe, S.; Kinoshita, M.; Hosokawa, T.; Morigaki, K.; Nakura, K. Capacity fade of LiAlyNi1-x-yCoxO 2 cathode for lithium-ion batteries during accelerated calendar and cycle life tests (surface analysis of LiAlyNi1-x-yCo xO2 cathode after cycle tests in restricted depth of discharge ranges). *J. Power Sources* **2014**, *258*, 210−217.

(24) Hwang, S.; Kim, S. M.; Bak, S. M.; Cho, B. W.; Chung, K. Y. Investigating Local Degradation and Thermal Stability of Charged Nickel-Based Cathode Materials through Real-Time Electron Microscopy. *ACS Appl. Mater. Interfaces* **2014**, *6*, 15140−15147.

(25) Shikano, M.; et al. Investigation of positive electrodes after cycle testing of high-power Li-ion battery cells II. An approach to the power fading mechanism using hard X-ray photoemission spectroscopy. *J. Power Sources* **2007**, *174*, 795−799.

(26) Makimura, Y.; Zheng, S.; Ikuhara, Y.; Ukyo, Y. Microstructural Observation of LiNi0.8Co0.15Al0.05O2 after Charge and Discharge by Scanning Transmission Electron Microscopy. *J. Electrochem. Soc.* **2012**, *159*, A1070−A1073.

(27) Sallis, S.; et al. Surface degradation of Li1-xNi0.80Co0.15Al0.05O2 cathodes: Correlating charge transfer impedance with surface phase transformations. *Appl. Phys. Lett.* **2016**, *108*, 263902.

(28) Tsujikawa, T.; Yabuta, K.; Matsushita, T.; Arakawa, M.; Hayashi, K. A Study on the Cause of Deterioration in Float-Charged Lithium-

DOI: 10.1021/acs.langmuir.7b00863
Langmuir 2017, 33, 9333−9353

Ion Batteries Using LiMn2O4 as a Cathode Active Material. *J. Electrochem. Soc.* **2011**, *158*, A322−A325.
(29) Nonaka, T.; Okuda, C.; Seno, Y.; Koumoto, K.; Ukyo, Y. X-ray absorption study on LiNi0.8Co0.15Al0.05O2 cathode material for lithium-ion batteries. *Ceram. Int.* **2008**, *34*, 859−862.
(30) Xia, H.; Lu, L.; Meng, Y. S.; Ceder, G. Phase Transitions and High-Voltage Electrochemical Behavior of LiCoO[sub 2] Thin Films Grown by Pulsed Laser Deposition. *J. Electrochem. Soc.* **2007**, *154*, A337.
(31) Lin, F.; et al. Surface reconstruction and chemical evolution of stoichiometric layered cathode materials for lithium-ion batteries. *Nat. Commun.* **2014**, *5*, 3529.
(32) Chen, K.; Unsworth, G.; Li, X. Measurements of heat generation in prismatic Li-ion batteries. *J. Power Sources* **2014**, *261*, 28−37.
(33) Saito, Y.; et al. Comparative study of thermal behaviors of various lithium-ion cells. *J. Power Sources* **2001**, *97*−*98*, 688−692.
(34) Saito, Y.; Shikano, M.; Kobayashi, H. Heat generation behavior during charging and discharging of lithium-ion batteries after long-time storage. *J. Power Sources* **2013**, *244*, 294−299.
(35) Kobayashi, Y.; et al. Precise Electrochemical Calorimetry of LiCoO2/Graphite Lithium-Ion Cell. *J. Electrochem. Soc.* **2002**, *149*, A978−A982.
(36) Lu, W.; Belharouak, I.; Vissers, D.; Amine, K. In Situ Thermal Study of Li1+xNi1/3Co1/3Mn1/31−xO2 Using Isothermal Microclorimetric Techniques. *J. Electrochem. Soc.* **2006**, *153*, A2147.
(37) Bang, H.; Yang, H.; Sun, Y. K.; Prakash, J. In Situ Studies of LixMn2O4 and LixAl0.17]Mn1.83O3.97S0.03 Cathode by IMC. *J. Electrochem. Soc.* **2005**, *152*, A421.
(38) Downie, L. E.; Dahn, J. R. Determination of the Voltage Dependence of Parasitic Heat Flow in Lithium Ion Cells Using Isothermal Microcalorimetry. *J. Electrochem. Soc.* **2014**, *161*, A1782−A1787.
(39) Rao, L. Heat-Generation Rate and General Energy Balance for Insertion Battery Systems. *J. Electrochem. Soc.* **1997**, *144*, 2697.
(40) Bernardi, D. A General Energy Balance for Battery Systems. *J. Electrochem. Soc.* **1985**, *132*, 5.
(41) Thomas, K. E.; Newman, J. Heats of mixing and of entropy in porous insertion electrodes. *J. Power Sources* **2003**, *119*−*121*, 844−849.
(42) Thomas, K. E.; Newman, J. Thermal Modeling of Porous Insertion Electrodes. *J. Electrochem. Soc.* **2003**, *150*, A176−A192.
(43) Srinivasan, R.; Carson Baisden, a.; Carkhuff, B. G.; Butler, M. H. The five modes of heat generation in a Li-ion cell under discharge. *J. Power Sources* **2014**, *262*, 93−103.
(44) Lu, W.; Prakash, J. In Situ Measurements of Heat Generation in a Li/Mesocarbon Microbead Half-Cell. *J. Electrochem. Soc.* **2003**, *150*, A262−A266.
(45) Lu, W.; Belharouak, I.; Liu, J.; Amine, K. Thermal properties of Li4/3Ti5/3O4/LiMn2O4 cell. *J. Power Sources* **2007**, *174*, 673−677.
(46) Miyashiro, H.; et al. Improvement of Degradation at Elevated Temperature and at High State-of-Charge Storage by ZrO2 Coating on LiCoO2. *J. Electrochem. Soc.* **2006**, *153*, A348−A353.
(47) Joachin, H.; Kaun, T. D.; Zaghib, K.; Prakash, J. Electrochemical and Thermal Studies of Carbon-Coated LiFePO4 Cathode. *J. Electrochem. Soc.* **2009**, *156*, A401−A406.
(48) Yang, H.; Prakash, J. Determination of the Reversible and Irreversible Heats of a LiNi0.8Co0.15Al0.05O2/Natural Graphite Cell Using Electrochemical-Calorimetric Technique. *J. Electrochem. Soc.* **2004**, *151*, A1222−A1229.
(49) Lu, W.; Yang, H.; Prakash, J. Determination of the reversible and irreversible heats of LiNi 0.8Co0.2O2/mesocarbon microbead Li-ion cell reactions using isothermal microcalorimetery. *Electrochim. Acta* **2006**, *51*, 1322−1329.
(50) Li, J.; Downie, L. E.; Ma, L.; Qiu, W.; Dahn, J. R. Study of the Failure Mechanisms of LiNi0.8Mn0.1Co0.1O2 Cathode Material for Lithium Ion Batteries. *J. Electrochem. Soc.* **2015**, *162*, A1401−A1408.
(51) Downie, L. E.; Hyatt, S. R.; Dahn, J. R. The Impact of Electrolyte Composition on Parasitic Reactions in Lithium Ion Cells Charged to 4.7 V Determined Using Isothermal Microcalorimetry. *J. Electrochem. Soc.* **2016**, *163*, A35−A42.
(52) van Bommel, A.; Krause, L. J.; Dahn, J. R. Investigation of the Irreversible Capacity Loss in the Lithium-Rich Oxide Li[Li1/5Ni1/5Mn3/5]O2. *J. Electrochem. Soc.* **2011**, *158*, A731.
(53) Downie, L. E.; Nelson, K. J.; Petibon, R.; Chevrier, V. L.; Dahn, J. R. The Impact of Electrolyte Additives Determined Using Isothermal Microcalorimetry. *ECS Electrochem. Lett.* **2013**, *2*, A106−A109.
(54) Downie, L. E.; Hyatt, S. R.; Wright, A. T. B.; Dahn, J. R. Determination of the Time Dependent Parasitic Heat Flow in Lithium Ion Cells Using Isothermal Microcalorimetry. *J. Phys. Chem. C* **2014**, *118*, 29533−29541.
(55) Ma, L.; et al. Ternary and Quaternary Electrolyte Additive Mixtures for Li-Ion Cells That Promote Long Lifetime, High Discharge Rate and Better Safety. *J. Electrochem. Soc.* **2014**, *161*, A1261−A1265.
(56) Hagh, N. M.; Cosandey, F.; Rangan, S.; Bartynski, R.; Amatucci, G. G. Electrochemical Performance of Acid-Treated Nanostructured LiMn 1.5Ni0.5O4−δ Spinel at Elevated Temperature. *J. Electrochem. Soc.* **2010**, *157*, A305−A319.
(57) Hagh, N. M.; Amatucci, G. G. Effect of cation and anion doping on microstructure and electrochemical properties of the LiMn1.5-Ni0.5O4-δ spinel. *J. Power Sources* **2014**, *256*, 457−469.
(58) Tarascon, J. M.; Gozdz, A. S.; Schmutz, C.; Shokoohi, F.; Warren, P. C. Performance of Bellcore's plastic rechargeable Li-ion batteries. *Solid State Ionics* **1996**, *86*−*88*, 49−54.
(59) Kobayashi, Y.; et al. Precise Electrochemical Calorimetry of LiCoO2/Graphite Lithium-Ion Cell. *J. Electrochem. Soc.* **2002**, *149*, A978.
(60) Watanabe, S.; Kinoshita, M.; Nakura, K. Capacity fade of LiNi(1-x-y)CoxAlyO 2 cathode for lithium-ion batteries during accelerated calendar and cycle life test. I. Comparison analysis between LiNi(1-x-y)Co xAlyO2 and LiCoO2 cathodes in cylindrical lithium-ion cells during long term storage test. *J. Power Sources* **2014**, *247*, 412−422.
(61) Van der Ven, A. First-Principles Evidence for Stage Ordering in Li[sub x]CoO[sub 2]. *J. Electrochem. Soc.* **1998**, *145*, 2149.
(62) Chang, C. Synthesis and electrochemical characterization of LiMO2 (M = Ni, Ni0.75Co0.25) for rechargeable lithium ion batteries. *Solid State Ionics* **1998**, *112*, 329−344.
(63) Pereira, N.; et al. Stoichiometric, Morphological, and Electrochemical Impact of the Phase Stability of LixCoO2. *J. Electrochem. Soc.* **2005**, *152*, A114−A125.
(64) Aurbach, D.; et al. An analysis of rechargeable lithium-ion batteries after prolonged cycling. *Electrochim. Acta* **2002**, *47*, 1899−1911.
(65) Kumai, K.; Miyashiro, H.; Kobayashi, Y.; Takei, K.; Ishikawa, R. Gas generation mechanism due to electrolyte decomposition in commercial lithium-ion cell. *J. Power Sources* **1999**, *81*−*82*, 715−719.
(66) du Pasquier, A.; et al. An update on the high temperature ageing mechanism in LiMn2O4 -based Li-ion cells. *J. Power Sources* **1999**, *81*−*82*, 54−59.
(67) Andersson, a. M.; et al. Surface Characterization of Electrodes from High Power Lithium-Ion Batteries. *J. Electrochem. Soc.* **2002**, *149*, A1358−A1369.
(68) Jarry, A.; et al. The Formation Mechanism of Fluorescent Metal Complexes at the LixNi0.5Mn1.5O4-δ/Carbonate Ester Electrolyte Interface. *J. Am. Chem. Soc.* **2015**, *137*, 3533−3539.
(69) Borodin, O.; Jow, T. R. Quantum Chemistry Studies of the Oxidative Stability of Carbonate, Sulfone and Sulfonate-Based Electrolytes Doped with BF4-, PF6- Anions. *ECS Trans.* **2010**, *33*, 77−84.
(70) Choi, N. S.; et al. Degradation of spinel lithium manganese oxides by low oxidation durability of LiPF6-based electrolyte at 60 °C. *Solid State Ionics* **2012**, *219*, 41−48.
(71) Bi, Y.; et al. Stability of Li2CO3 in cathode of lithium ion battery and its influence on electrochemical performance. *RSC Adv.* **2016**, *6*, 19233−19237.
(72) Robert, R.; Bünzli, C.; Berg, E. J.; Novák, P. Activation Mechanism of LiNi0.80Co0.15Al0.05O2: Surface and Bulk Operando

DOI: 10.1021/acs.langmuir.7b00863
Langmuir 2017, 33, 9333−9353

Electrochemical, Differential Electrochemical Mass Spectromet. *Chem. Mater.* **2015**, *27*, 526−536.
(73) Tasaki, K.; et al. Solubility of Lithium Salts Formed on the Lithium-Ion Battery Negative Electrode Surface in Organic Solvents. *J. Electrochem. Soc.* **2009**, *156*, A1019−A1027.
(74) Campion, C. L.; Li, W.; Lucht, B. L. Thermal Decomposition of LiPF6-Based Electrolytes for Lithium-Ion Batteries. *J. Electrochem. Soc.* **2005**, *152*, A2327−A2334.
(75) Ellis, L. D.; Xia, J.; Louli, A. J.; Dahn, J. R. Effect of Substituting LiBF4 for LiPF6 in High Voltage Lithium-Ion Cells Containing Electrolyte Additives. *J. Electrochem. Soc.* **2016**, *163*, A1686−A1692.
(76) Pereira, N.; Ruotolo, M. C.; Lu, M. Y.; Badway, F.; Amatucci, G. G. Elevated temperature performance of high voltage Li1+yMn1.5-Ni0.5O4−xFx spinel in window-shifted Li-ion cells. *J. Power Sources* **2017**, *338*, 145−154.
(77) Imhof, R.; Novak, P. Oxidative Electrolyte Solvent Degradation in Lithium-Ion Batteries - An In Situ Differential Electrochemical Mass Spectrometry Investigation. *J. Electrochem. Soc.* **1999**, *146*, 1702−1706.
(78) Mohanty, D.; et al. Modification of Ni-Rich FCG NMC and NCA Cathodes by Atomic Layer Deposition: Preventing Surface Phase Transitions for High-Voltage Lithium-Ion Batteries. *Sci. Rep.* **2016**, *6*, 1−16.

DOI: 10.1021/acs.langmuir.7b00863
Langmuir 2017, 33, 9333−9353